

RESEARCH ARTICLE

10.1002/2016JE005154

Key Points:

- Using mutually oriented subsamples of lunar troctolite 76535, we find further evidence for a dynamo on the Moon 4.25 Ga
- We find that the magnetizing field had a paleointensity of 20–40 microteslas
- New $^{40}\text{Ar}/^{39}\text{Ar}$ thermochronometry measurements provide an improved sample age estimate of 4249 (plus minus) 12 Ma

Supporting Information:

- Supporting Information S1

Correspondence to:

I. Garrick-Bethell,
igarrick@ucsc.edu

Citation:


Garrick-Bethell, I., B. P. Weiss, D. L. Shuster, S. M. Tikoo, and M. M. Tremblay (2016), Further evidence for early lunar magnetism from troctolite 76535, *J. Geophys. Res. Planets*, 121, doi:10.1002/2016JE005154.

Received 11 AUG 2016

Accepted 30 NOV 2016

Accepted article online 7 DEC 2016

Further evidence for early lunar magnetism from troctolite 76535

Ian Garrick-Bethell^{1,2}, Benjamin P. Weiss³, David L. Shuster^{4,5}, Sonia M. Tikoo⁶, and Marissa M. Tremblay^{4,5} 
¹Department of Earth and Planetary Sciences, University of California, Santa Cruz, Santa Cruz, California, ²School of Space Research, Kyung Hee University, Yongin-si, South Korea, ³Department of Earth, Atmospheric and Planetary Sciences, Massachusetts Institute of Technology, Cambridge, Massachusetts, USA, ⁴Department of Earth and Planetary Science, University of California, Berkeley, Berkeley, California, USA, ⁵Berkeley Geochronology Center, Berkeley, California, USA, ⁶Department of Earth and Planetary Sciences, Rutgers University, Piscataway Township, New Jersey, USA

Abstract The earliest history of the lunar dynamo is largely unknown and has important implications for the thermal state of the Moon and the physics of dynamo generation. The lunar sample with the oldest known paleomagnetic record is the 4.25 billion year old (Ga) troctolite 76535. Previous studies of unoriented subsamples of 76535 found evidence for a dynamo field with a paleointensity of several tens of microteslas. However, the lack of mutual subsample orientation prevented a demonstration that the magnetization was unidirectional, a key property of thermoremanent magnetization. Here we report further alternating field demagnetization on three mutually oriented subsamples of 76535, as well as new pressure remanent magnetization experiments to help rule out shock magnetization. We also describe new $^{40}\text{Ar}/^{39}\text{Ar}$ thermochronometry and cosmogenic neon measurements that better constrain the rock's thermal history. Although the rock is unbrecciated, unshocked, and slowly cooled, its demagnetization behavior is not ideal due to spurious remanence acquisition. Despite this limitation, all three subsamples record a high coercivity magnetization oriented in nearly the same direction, implying that they were magnetized by a unidirectional field on the Moon. We find no evidence for shock remanence, and our thermochronometry calculations show no significant reheating events since 4249 ± 12 million years ago (Ma). We infer a field paleointensity of approximately 20–40 μT , supporting the previous conclusion that a lunar dynamo existed at 4.25 Ga. The timing of this field supports an early dynamo powered by thermal or thermochemical core convection and/or a mechanical dynamo but marginally excludes a dynamo delayed by thermal blanketing from radiogenic element-rich magma ocean cumulates.

1. Introduction

During the Apollo era, there was considerable debate over the origin of magnetization observed in lunar rocks [Fuller and Cisowski, 1987]. However, recent lunar paleomagnetism studies [Cournède et al., 2012; Garrick-Bethell et al., 2009; Shea et al., 2012; Suavet et al., 2013; Tikoo et al., 2014; Weiss and Tikoo, 2014], dynamo and thermal evolution models [Dwyer et al., 2011; Laneuville et al., 2014; Le Bars et al., 2011; Scheinberg et al., 2015], and remote sensing studies [Arkani-Hamed and Boutin, 2014; Halekas et al., 2003; Hood et al., 2013; Takahashi et al., 2014] have offered new evidence supporting the hypothesis of a lunar dynamo. In particular, a dynamo epoch with Earth-strength fields from at least 3.72 to 3.56 Ga is supported by paleomagnetism studies [Shea et al., 2012; Suavet et al., 2013].

Garrick-Bethell et al. [2009] and Lawrence et al. [2008] examined the natural remanent magnetization (NRM) and thermal history of troctolite 76535. Troctolite 76535 is a monomict coarse-grained unshocked rock, with approximately equal modal abundances of plagioclase and olivine, with ~4–5% orthopyroxene [Gooley et al., 1974; McCallum and Schwartz, 2001]. It cooled slowly in the deep crust, at a depth of ~30–50 km, based on thermobarometry calculations [McCallum and Schwartz, 2001]. Upon excavation it likely cooled in a hot ejecta blanket from temperatures of $\approx 600^\circ\text{C}$, for ≈ 10 kyr [Garrick-Bethell et al., 2009]. The troctolite is a particularly important rock because among all unbrecciated and unshocked (<5 GPa) Apollo samples, it has the oldest known undisturbed $^{40}\text{Ar}/^{39}\text{Ar}$ age of 4.2–4.3 Ga (~100 Ma uncertainty is from Apollo-era measurements) [Husain and Schaeffer, 1975; Bogard et al., 1975; Huneke and Wasserburg, 1975], meaning that its NRM is the oldest identified paleomagnetic record from the Moon. In addition, the unshocked nature of 76535 and its

simple thermal history mean that its NRM should be a product of a long-lived ambient field, rather than transient fields generated by an impact event [Garrick-Bethell *et al.*, 2009].

Paleofield records for this early lunar epoch are of key importance because for a dry lunar interior [Konrad and Spohn, 1997; Laneuville *et al.*, 2013], a thermal convection dynamo is likely to have operated only prior to ≈ 4.1 Ga. Furthermore, different dynamo models predict various times for the onset of the lunar magnetic field. Stegman *et al.* [2003] and Zhang *et al.* [2013] showed that the onset of a thermal or thermochemical convection dynamo may have been delayed until ≈ 250 Ma after lunar magma ocean solidification. Because magma ocean solidification and overturn were likely completed between ≈ 4.47 and 4.32 Ga [Elkins-Tanton, 2012, Figure 8], the dynamo may therefore have been delayed until ≈ 4.2 –4.1 Ga. On the other hand, Dwyer *et al.* [2011] and Meyer and Wisdom [2011] suggested that mechanical stirring could power a dynamo after the Moon reached a semimajor axis > 26 –29 Earth radii. This corresponds to only ≈ 100 –200 Ma after accretion (using Figure S2 of Dwyer *et al.* [2011]), suggesting a dynamo possibly operating as early as ≈ 4.4 Ga. A more precise age for the NRM in 76535 would help distinguish amongst these models.

Garrick-Bethell *et al.* [2009] found that four unoriented subsamples of 76535 carried three NRM components. The observed low coercivity (LC) component unblocked below 15 mT, which is likely an isothermal remanent magnetization (IRM) acquired following sampling on the Moon. Medium coercivity (MC) and high coercivity (HC) components were inferred to be unblocked over 30 to 80 mT and > 80 mT, respectively. The high peak alternating field (AF) for these components and their low efficiencies (NRM/IRM ≈ 0.02) indicated that they are unlikely to be secondary IRM or viscous remanent magnetization (VRM). Although the four subsamples studied were not mutually oriented, the angular difference between the MC and HC directions was similar within each subsample ($\approx 146^\circ$), implying that these components had the same origins and were acquired in a uniform field. Using thermochronometry calculations, Garrick-Bethell *et al.* [2009] interpreted the MC and HC magnetizations to have formed during two thermal events on the Moon. Using anhysteretic remanent magnetization (ARM) and IRM paleointensity methods [Gattacceca and Rochette, 2004; Stephenson and Collinson, 1974], they obtained mean paleointensities of $12 \pm 2 \mu\text{T}$ and $32 \pm 6 \mu\text{T}$, respectively, for the MC component and $43 \pm 7 \mu\text{T}$ and $140 \pm 30 \mu\text{T}$, respectively, for the HC component (uncertainties are 95% confidence intervals from the regression analysis only and do not include the variability of efficiencies of thermoremanence compared to IRM and ARM in different rock types).

Given the importance of troctolite 76535 for understanding the history of lunar magnetism, we have performed additional experiments to further test and refine the above conclusions. In particular, a key test of the dynamo hypothesis for lunar paleomagnetism is that mutually oriented subsamples should be magnetized in nearly the same direction because dynamo fields are spatially constant over kilometer scales (much larger than the 5 cm size of the original 76535 parent sample).

The paleomagnetism of troctolite 76535 is challenging to analyze. The presence of the IRM LC component, which should overprint a wide range of unblocking temperatures, limits the accuracy of thermal paleointensity experiments [Lawrence *et al.*, 2008]. During AF demagnetization, the sample acquires spurious ARM and gyroremanent magnetization (GRM), which increasingly obscures the underlying NRM. A further key limitation faced by the Garrick-Bethell *et al.* [2009] study was that they did not have access to large, mutually oriented subsamples, such that they were only able to compare the relative angular difference between NRM components across the subsamples. Garrick-Bethell *et al.* [2009] did study two mutually oriented samples (76535,138,2 and 76535,138,2, see their supporting information section 5), but one sample was very small (22 mg), difficult to orient for anisotropy measurements, susceptible to GRM, and had poor AF demagnetization behavior. A possible HC component was identified, but the poor AF demagnetization behavior prevented any definitive conclusions. Furthermore, no MC component could be identified.

The analysis of three, larger mutually oriented subsamples is the main goal of the current study. We also present the first laboratory pressure remanent magnetization (PRM) experiments on 76535, which help rule out the possibility that its NRM is due to a shock remanent magnetization (SRM). We also describe new estimates of the minimum paleointensity recording limit for 76535 using ARM experiments, revising those of Tikoo *et al.* [2012].

Finally, we present results of modern $^{40}\text{Ar}/^{39}\text{Ar}$, $^{38}\text{Ar}/^{37}\text{Ar}$, and cosmogenic neon measurements and thermochronometry calculations to better constrain the age of the NRM. A more accurate age could discriminate between various lunar dynamo models with differing predictions for the onset time of the lunar field. The new high-accuracy temperature measurements also enable us to better constrain the permissible thermal histories of the sample.

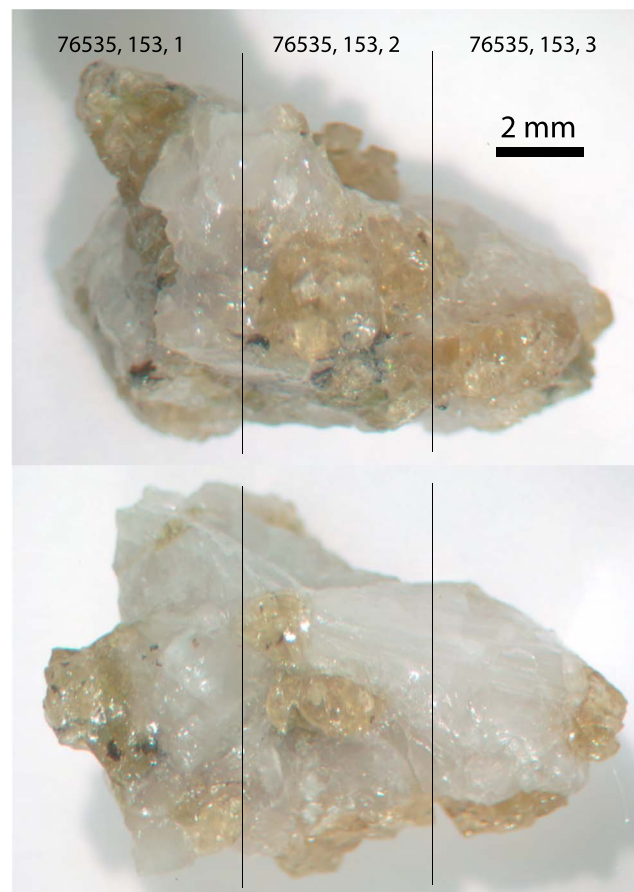


Figure 1. Photographs of two opposite faces of 76535, 153. Lines indicate the approximate sizes and locations of subsamples 1, 2, and 3.

Paleomagnetism Laboratory. The three subsamples were subjected to static three-axis alternating field (AF) demagnetization and measured with a 2G Enterprises 755 Superconducting Rock Magnetometer (sensitivity $\sim 10^{-12}$ Am²) in a shielded room (< 200 nT DC field). Demagnetization experiments were performed using the Zijderveld-Dunlop GRM-correction method [Stephenson, 1993]. Specifically, we demagnetized each of the samples in the magnetometer x , y , z , x , and y axes (in that order) and calculated the mean of the last three measurements. In addition, we performed repeat AF measurements at a single field level to average out the effects of spurious ARM (which appears randomly oriented in the AF equipment). The repeat measurements were averaged to produce a single measurement for each AF level (Tables S1–S3 in the supporting information). No running averages over different AF levels were performed, in contrast to Garrick-Bethell *et al.* [2009]. To demonstrate that the measured NRMs do not depend on the orientation of the samples with respect to the magnetometer axes, subsample 1 was measured in the magnetometer frame in a position inverted with respect to the other two subsamples; its demagnetization data were then rotated 180° into the same frame as the other two subsamples.

After demagnetization, principal component analysis (PCA) was used to identify the magnetization components and their directions [Kirschvink, 1980]. To qualitatively determine if the HC component decays to the origin, we determined the distance between the first point of a PCA fit not forced through the origin and the direction of the unconstrained fit (i.e., a measure of the component's deviation angle from the origin, known as the dANG value) [Tauxe and Staudigel, 2004]. If the dANG value is less than the maximum angular deviation (MAD) of the PCA fit, we conclude that the component decays to the origin. In that case, it is therefore a candidate for the primary NRM acquired during cooling on the Moon [Garrick-Bethell *et al.*, 2009; Lawrence *et al.*, 2008]. We then perform a line fit forced through the origin to obtain the reported HC direction.

2. Methods

2.1. Magnetism

We subdivided a 574 mg parent sample (76535,153) into three mutually oriented pieces of masses 200 mg, 150 mg, and 120 mg (Figure 1, hereafter referred to as subsamples 1, 2, and 3, respectively). These samples are not mutually oriented with respect to the samples in Garrick-Bethell *et al.* [2009]. Subsample 2 was cut from the rock between subsamples 1 and 3. The cutting was accomplished using a low speed Buhler Isomet wafering saw that had been previously demonstrated not to significantly remagnetize weakly magnetized materials [Garrick-Bethell *et al.*, 2009]. Prior to cutting, the parent sample was infused with nonmagnetic cyanoacrylate cement to prevent crumbling. The three subsamples were glued to nonmagnetic quartz discs with cyanoacrylate, with angular orientation errors estimated to be $< 10^\circ$. All subsample measurements are reported in the same mutually oriented reference frame.

All paleomagnetic measurements were acquired in the Massachusetts Institute of Technology (MIT)

We obtained paleointensity estimates for each component using AF demagnetization of IRM and ARM following the methods of *Garrick-Bethell et al.* [2009]. We calculate the NRM, ARM, and IRM lost using vector subtraction, starting at the first demagnetization step for the relevant magnetization component (known as the REM' method) [Gattacceca and Rochette, 2004]. In the previous study *Garrick-Bethell et al.* [2009] used ARM gained, but here we use ARM lost. We estimate the ARM and IRM paleointensity via

$$\begin{aligned} \text{ARM paleointensity in } \mu\text{T} &= (\Delta\text{NRM}/\Delta\text{ARM})/f' \times (\text{bias field in } \mu\text{T}) \\ \text{IRM paleointensity in } \mu\text{T} &= (\Delta\text{NRM}/\Delta\text{IRM}) \times a, \end{aligned} \quad (1)$$

where f' is the ratio of thermoremanent magnetization (TRM) to ARM and a is a coefficient with units of μT that is inversely proportional to the TRM/IRM ratio. ΔNRM , ΔARM , ΔIRM are, respectively, the vector-subtracted loss or gain of NRM, ARM, and IRM. We assume that $f' = 1.34$ [Stephenson and Collinson, 1974], and $a = 3000 \mu\text{T}$ [Gattacceca and Rochette, 2004]. The exact values of these ratios depend on the samples' grain size and shape distributions. *Weiss and Tikoo* [2014] describe how the two-standard-deviation uncertainties on paleointensities estimated in this manner are typically a factor of 2–3 for iron-nickel-bearing samples.

To correct our PCA fit directions and paleointensity estimates for anisotropy, we determined the IRM anisotropy ellipsoids, and P and T values (degree of anisotropy [Nagata, 1961] and anisotropy shape factor [Jelinek, 1981], respectively) of each sample by giving the rock orthogonal 250 mT IRMs and using the methods described in *Garrick-Bethell et al.* [2009]. If magnetic carriers have multiple easy axes, then using low-field IRMs to assess anisotropy can be biased by the sample's IRM history [Mitra et al., 2011]. However, in our case this is not a concern because (i) the IRM field we use is relatively strong compared to the fields used by *Mitra et al.* [2011] (when normalized by the carrier's saturation remanence), (ii) kamacite, the magnetic carrier in 76535 [Garrick-Bethell et al., 2009] is dominated by shape anisotropy [Garrick-Bethell and Weiss, 2010] and therefore unlikely to have multiple easy axes, and (iii) we AF demagnetize each IRM after applying it, such that it cannot bias the remanence of the next IRM.

PRM acquisition experiments were performed on subsample 2 following *Shea et al.* [2012], *Suavet et al.* [2013], and *Bezaeva et al.* [2010]. Subsample 2 was pressurized in a nonmagnetic pressure cell similar to the design described in *Sadykov et al.* [2008]. A coil surrounding the pressure cell applied a 800 μT DC field, while pressure was applied using a Specac manual hydraulic press. The sample was held at the peak pressure for at least 1 min. Experiments were conducted for peak pressures of 0.45, 0.9, 1.35, and 1.8 GPa. After each PRM acquisition, the sample was stepwise AF demagnetized following the Zijderveld-Dunlop protocol up to 85 mT.

2.2. $^{40}\text{Ar}/^{39}\text{Ar}$ and $^{38}\text{Ar}/^{37}\text{Ar}$ Thermochemistry

To constrain the age of the NRM in 76535, we conducted stepwise-degassing $^{40}\text{Ar}/^{39}\text{Ar}$ and $^{38}\text{Ar}/^{37}\text{Ar}$ thermochemistry. Two ~ 3 mg whole-rock aliquots were subjected to feedback-controlled laser heating following previously described procedures [Cassata et al., 2009; Shea et al., 2012; Shuster et al., 2010] (supporting information Appendix A2 and Table S4). We report the apparent $^{40}\text{Ar}/^{39}\text{Ar}$ age observed at each extraction step relative to the Hb3gr neutron fluence monitor and use the monitor age (~ 1081 Ma) and decay constants of *Renne et al.* [2011] and *Renne et al.* [2010] and Ar isotopic abundances of *Steiger and Jager* [1977].

2.3. Cosmogenic Neon Thermochemistry

To constrain the thermal history of 76535 during its exposure at the lunar surface and corroborate thermal histories inferred from Ar measurements, we conducted a diffusion experiment and measurements of cosmogenic Ne in anorthite grains from 76535. For the diffusion experiment, we measured ^{21}Ne and ^{22}Ne in a neutron-irradiated fragment of 76535 anorthite subjected to feedback-controlled laser heating (supporting information Appendix A3 Table S5). For the cosmogenic neon measurements, we measured ^{20}Ne , ^{21}Ne , and ^{22}Ne in five unirradiated anorthite grains using the same feedback-controlled laser system (supporting information Appendix A3 and Table S6). Because Ne has a higher diffusivity than Ar at lunar surface temperatures, it can provide a more accurate constraint on the extent of solar heating.

3. Results and Interpretation

3.1. AF Demagnetization

3.1.1. Subsample 1

Subsample 1 has an LC component removed by 15 mT (Figure 2a and Table 1). After removal of the LC component, the NRM moves to two clusters of stable magnetization directions in the AF ranges of 15–145 mT and

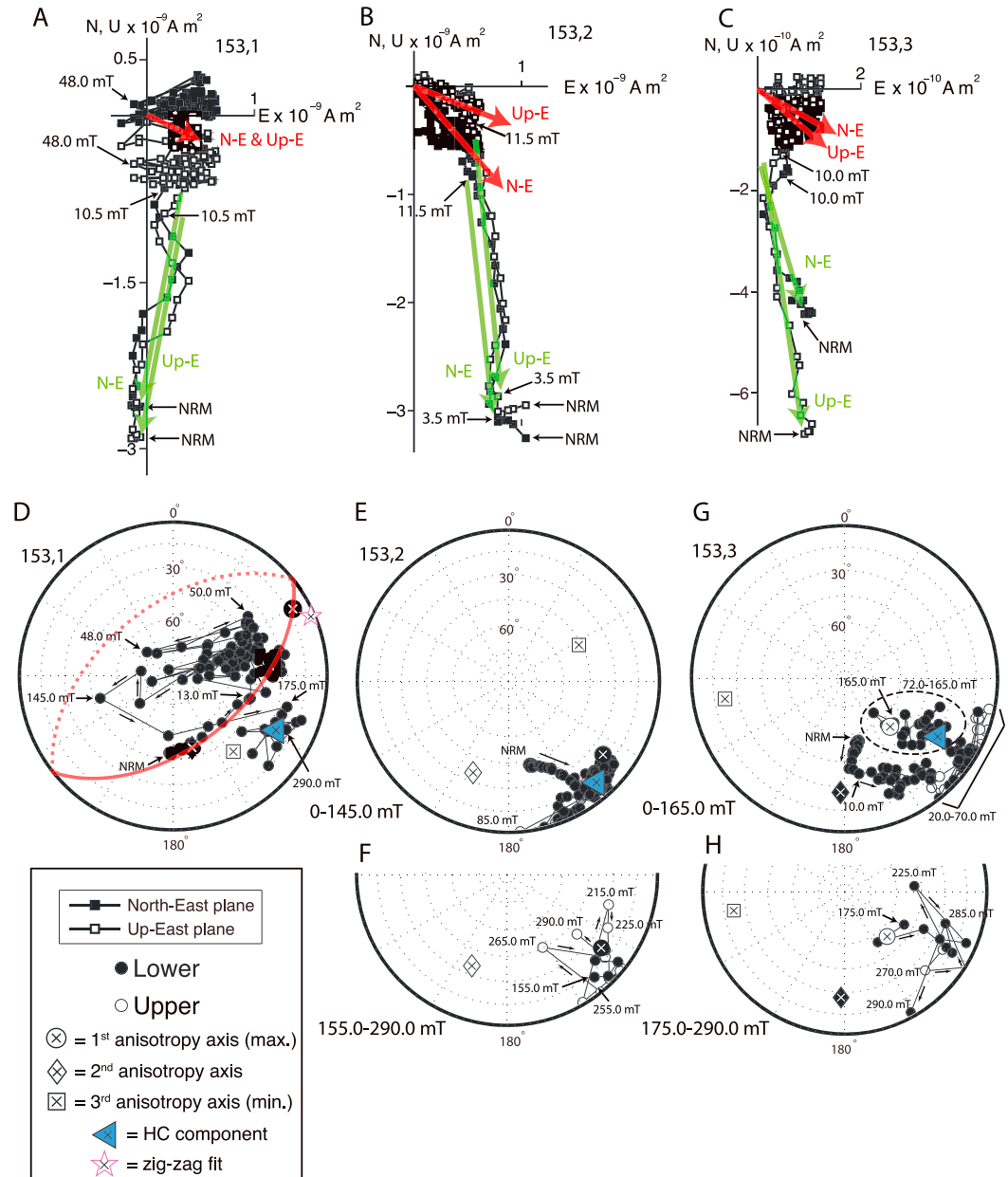


Figure 2. AF demagnetization of three mutually oriented pieces of 76535,153. (a–c) Orthographic projections of subsamples 1, 2, and 3. Green and red lines show the directions of the LC and HC components, respectively (see Table 1). Only one red line is shown in Figure 2a due to the very close overlap between the two projections of the HC best fit line in the Z-E and N-E planes. The start of the 72.0 mT cluster for subsample 3 is indicated by the circular dashed line in Figure 1g. In Figures 2a–2c, closed and open symbols represent projections onto the north-east and up-east planes, respectively. (d) Equal area stereographic projection showing magnetization directions for subsample 1 during AF demagnetization. The red great circle is the plane defined by the easy-intermediate axes. (e and f) Equal area projection for subsample 2. AF points above 155.0 mT are highlighted in Figure 2f. (g and h) Equal area projection for subsample 3. AF points above 175.0 mT are highlighted in Figure 2h. In Figures 2d–2f, the large circles, diamonds, and squares indicate the largest, intermediate, and smallest anisotropy ellipsoid axes, respectively. The star in Figure 2d indicates the direction from the zig-zag fit (see section 3). The paleomagnetic data shown here are not anisotropy corrected. In Figures 2d–2h, open and closed symbols represent projections on upper and lower hemispheres, respectively.

Table 1. Summary of PCA Fits

Component or Behavior	AF Steps (mT)	Dec (°), Inc (°) (Corrected) ^a	MAD (°) ^b	N ^c	Type
<i>Sample 1</i>					
LC	0–10.5	190.8, 45.4	5.9	20	Line
Zigzag	42.0–50.0	246.5, –2.3	12.1	9	Line
HC	175.0–290.0	117.8, 25.1 (124.4, 16.3)	40.5/11.1	12	Line through origin (dANG = 1.7°)
<i>Sample 2</i>					
LC	3.5–11.5	174.2, 47.4	3.5	17	Line
HC	15.0–225.0	138.3, 11.8 (142.2, 7.6)	25.8/8.5	95	Line through origin (dANG = 10.7°)
<i>Sample 3</i>					
LC	0–10.0	162.7, 64.1	4.6	19	Line
HC	175.0–290.0	120.5, 28.9 (118.0, 29.8)	32.3/27.3	12	Line through origin (dANG = 44.5°)

^aCorrected for anisotropy using IRM 250.0 mT.^bFor HC components, MAD is shown for a fit not forced through the origin/forced through the origin.^cN = number of points in fit.

>175 mT (Figure 2d). The remanence in both clusters does not decay appreciably. These two clusters and the lack of decay suggest there are at least two NRM components (within the great circle connecting the clusters) that are not readily removed, with one possibly representing the MC component previously identified by Garrick-Bethell *et al.* [2009] (see below and section 4). However, in the coercivity range of the 15–145 mT cluster, some zig-zag motion of the magnetization also appears. This zig-zag behavior consists of magnetization directions that oscillate between points that lie approximately on a great circle. To test that this behavior is controlled by the rock's remanence anisotropy easy axis [Tikoo *et al.*, 2012], we conducted a PCA line fit over the coercivity range over which the zig-zag motion takes place. The fit direction is essentially indistinguishable (11° away, which is less than the fit direction's MAD of 12.1°) from the anisotropy easy axis (Figure 2d, Table 1). In addition, the anisotropy of this sample (degree $P = 1.7$) is the highest of the three subsamples and higher than that of most lunar rocks (compare with Figure 8 of Tikoo *et al.* [2012]). Together, these observations suggest that the zig-zag behavior is indeed controlled by the sample's anisotropy, making the precise identification of any component in this coercivity range difficult.

An MC component in this subsample is suggested by the clustered magnetization directions in the 15–145 mT range and the approximately great circle path from 145 to 175 mT. However, the demagnetization behavior is nonideal. In the supporting information in Appendix A1 we describe evidence from these data that an MC component may exist. However, for the HC component, which is the most important part of our analysis, we focus on the final cluster of magnetization directions from 175.0 to 290.0 mT. The magnetization does not appreciably decay in this coercivity range (the mean is $4.6 \times 10^{-10} \text{ Am}^2$, fluctuating with a standard deviation of $1 \times 10^{-10} \text{ Am}^2$), likely due to spurious ARM acquisition and/or unmitigated GRM effects (see section 4), but we do find that $d\text{ANG} < \text{MAD}$. Unfortunately, the negligible amount of NRM decay means that we cannot infer a paleointensity estimate from the HC component for this subsample over the HC range (although the ratio of NRM demagnetized to 20 mT, to saturation IRM is 0.02, indicating a “residual” paleointensity [Cisowski *et al.*, 1983] of $\approx 60 \mu\text{T}$). Nevertheless, an HC component is likely present since its direction is very similar (nearly within the MAD values) of the HC directions inferred from the other two subsamples (see Figure 4 and sections 3.1.2 and 3.1.3). Therefore, we perform a line fit forced through the origin to obtain the best estimate of the subsample's HC direction (Table 1 and Figures 2a and 4). Finally, we note that if we consider the subsample's measurements in the magnetometer coordinate system (i.e., not converted into the coordinate system of the other two samples by inverting it; see section 2), its HC component would have a declination of 27.8° and inclination of –25.1°, instead of 117.8° and 25.1°, respectively (not correcting for anisotropy). Because the arc distance between these two directions is 100.3°, the uniformity of the HC component directions across the three subsamples cannot be ascribed to an artifact of the AF demagnetization process.

3.1.2. Subsample 2

AF demagnetization of subsample 2 removed a small amount (9%) of remanence up to 3.5 mT. Because the remanence in this range has a unique direction compared to the remanence above 3.5 mT and has a low ratio

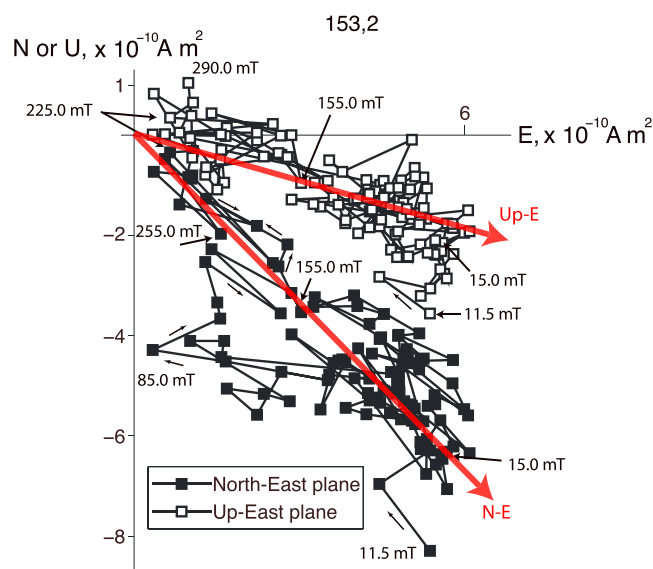


Figure 3. Zoom in of the orthographic projection of AF demagnetization of subsample 2 starting at 11.5 mT (see Figure 1). The red lines show the HC component direction. The data shown here are not anisotropy corrected. Closed and open symbols represent projections onto the northeast and up east planes, respectively.

of ΔNRM to ΔIRM (0.04), we interpret it to be a VRM acquired in the Earth's field. Like subsample 1, subsample 2 also exhibits a LC component that is removed by approximately 11 mT and has high $\Delta\text{NRM}/\Delta\text{IRM}$ (0.25) (Figure 2b) and so is likely an IRM overprint.

Unlike subsample 1, subsample 2 appears to have only one additional component (no obvious evidence for an MC component could be inferred). This HC component decays to the origin starting from ≈ 15 mT (i.e., $d\text{ANG} < \text{MAD}$). During AF demagnetization, the sample directions deviate slightly in declination at 85 mT and return to the previous direction by 155 mT (Figure 3). This deviation may be due to spurious ARM.

Above 225 mT, the remanence displays some minor zig-zag behavior toward and away from the easy axis, presumably after the removal of most of the NRM. Above ~ 155.0 mT the magnetization begins to move more erratically, presumably due to increased ARM noise (Figure 2f). To obtain the HC component, we performed a line fit (forced through the origin) from 15–225 mT.

3.1.3. Subsample 3

Subsample 3 also exhibits an LC component that is removed by approximately 11 mT (Figure 2c) and is likely an IRM. After the LC component is removed, the magnetization forms a cluster of stable directions from approximately 20 to 70 mT and then another cluster from approximately 72 to 290 mT (Figure 2h).

The NRM magnitude remains nearly constant from 72 to ≈ 165 mT (usually varying by $\pm \sim 10\%$ between demagnetization steps), after which it decays by a factor of 2 from 175 to 290 mT. Performing a line fit starting at either 72 or 175 mT produces fits with similar directions (within 13° of each other). While this subsample can be considered in some sense to decay to the origin, the motion to the origin is not as clear ($d\text{ANG} > \text{MAD}$), and it does not occur over as wide a range of coercivity as for subsample 2. However, as for subsample 1, since the HC components in all three subsamples are in the same direction, we infer that this is the final HC component and perform a line fit forced through the origin.

3.1.4. Mean Directions of LC and HC

While the mean LC direction does not fall within the LC MADs of any sample and none of the LC components fall within each other's MADs, the LC directions are closely clustered (angular standard deviation $\theta_{63} = 13.2^\circ$ and Fisher precision parameter $k = 38$; Figure 4). This suggests the LC component was acquired in a field that was approximately unidirectional over the length scale of the subsamples.

The HC directions were anisotropy corrected using IRM anisotropy ellipsoids. Like the LC components, the HC components are also closely clustered ($\theta_{63} = 16.4^\circ$, $k = 25$ for corrected directions; Figure 4). Subsample 2's easy axis is close (19.9°) to its HC direction, but the other two subsample easy axes are located far (61.7° for subsample 1 and 85.7° for subsample 3) from their HC directions (Figure 4) (note the maximum distance is 90°). Therefore, it is unlikely that the HC component in 76535 is an artifact of anisotropy. In summary, due to the similarity of the HC component directions, it is likely that these three subsamples acquired their most stable remanence component in a unidirectional field.

3.2. Anisotropy of Remanence

The subsamples have IRM anisotropy P values ranging from 1.3 to 1.7 (Table 2). Subsample 1 is the only subsample with a shape parameter, T , that is positive, which indicates that its anisotropy ellipsoid is an oblate

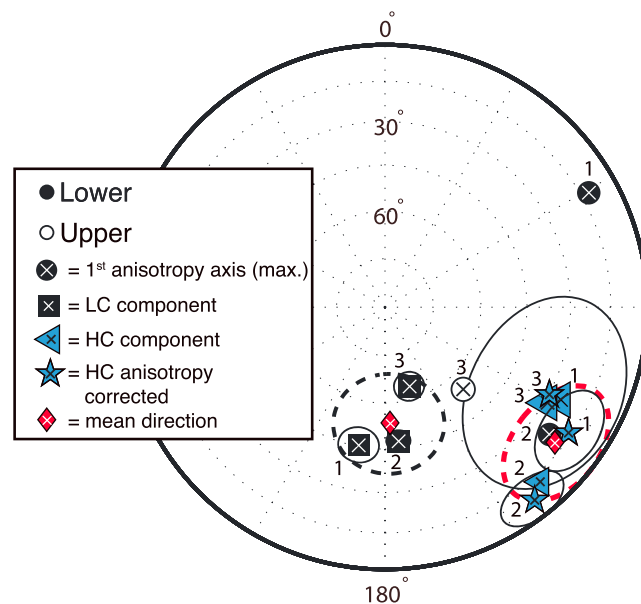


Figure 4. Equal area stereographic projections of LC and HC directions for each subsample (see Table 1). The anisotropy-corrected directions of the HC components are shown as stars, and the mean direction of these HC directions is also shown. The HC components are clustered with angular standard deviation $\theta_{63} = 16.4^\circ$ (Fisher precision parameter $k = 25$). The easy anisotropy axes for each subsample are shown as circles. The numbers near each point indicate the subsample number. The MAD values for the anisotropy-corrected HC directions are shown as circles around each star, and the angular standard deviation of the mean LC and HC directions are shown as dashed black and red lines, respectively. Open and closed symbols represent projections on upper and lower hemispheres, respectively.

inferred to have an IRM blocked up to ≈ 11.0 mT (the LC component), similar to that observed in this study. Therefore, we focus on the HC remanence lost starting from 15.0 mT (slightly higher than 11.0 mT to provide some margin) as the fraction of the NRM that is likely a TRM (Figure 5b).

3.3.1. Comparison of NRM With IRM

The AF demagnetization behavior of the NRM and a strong (250 mT) laboratory IRM differ substantially (Figure 5a). The peak IRM intensity is higher than that of the NRM by an order of magnitude, and the shape of the IRM demagnetization curve is concave up. Therefore, as in our previous study, we conclude that it is highly unlikely that the HC remanence in subsample 2 is due to an IRM acquired in a comparable field.

3.3.2. Comparison of NRM With ARM

We compared the NRM to an ARM produced with a $50 \mu\text{T}$ bias field and 250 mT AC field (as an analog for TRM formed in a field with intensity similar to that inferred for the NRM; see section 3.4). Both NRM and ARM demagnetize slightly up to 3.5 mT (Figure 5a). As discussed in section 3.1.2, this portion of the NRM is likely due to a VRM acquired in the Earth's field.

spheroid (the other samples have prolate spheroids). The origin of the anisotropy in all three subsamples is unknown, but it is presumably due to large, irregular interstitial metal grains and/or the large silicate crystal sizes (often > 1 mm) which are known to contain oriented ferromagnetic inclusions [Gooley *et al.*, 1974; Nord, 1976].

3.3. Behavior of AF of NRM Compared With AF of IRM, ARM, and PRM

Garrick-Bethell *et al.* [2009] used comparisons of AF demagnetization of laboratory magnetizations to infer that the MC and HC components are TRMs [see also Fu *et al.*, 2012; Shea *et al.*, 2012]. However, they did not make comparisons with AF demagnetization of PRM to determine if the NRM was a shock remanent magnetization (SRM). Therefore, we now reassess these comparisons with a new understanding of the AF of PRM behavior.

We focus on subsample 2 because among the three subsamples, it exhibits the clearest HC component. As discussed in Garrick-Bethell *et al.* [2009] and section 3.1, the NRM of 76535 was

Above 15 mT (the start of the HC component), similar amounts of remanence are removed for both ARM and NRM, indicating that the NRM behaves like an ARM (e.g., between 15.0 and 25.0 mT, $\approx 0.3 \times 10^{-9} \text{ Am}^2$ is lost for ARM and NRM, and between ≈ 25 and ≈ 85 mT, another $\sim 0.2 \times 10^{-9} \text{ Am}^2$ are lost for ARM and NRM; Figure 5b).

Table 2. Mass and IRM Anisotropy Data for 76535, 153

Subsample	Mass (mg)	P^a	T^b
1	200	1.7	0.5
2	150	1.5	−0.8
3	120	1.3	−0.5

^aDegree of anisotropy.

^bShape factor.

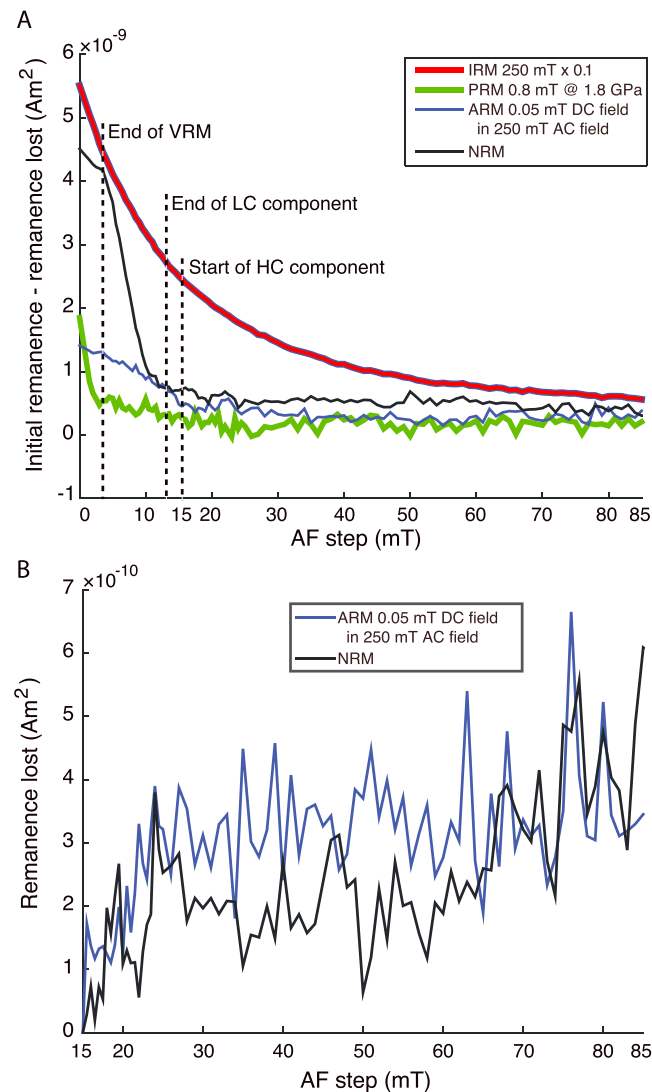


Figure 5. AF demagnetization of different forms of remanence for subsample 2. In both panels, the remanence lost is calculated by vector subtraction. (a) AF of NRM (black), AF of PRM in a field of 0.8 mT applied at a pressure of 1.8 GPa (green), AF of ARM with bias field of 0.05 mT applied in a peak AC field of 250 mT (blue), and AF of an IRM acquired in a field of 250 mT (red) multiplied by 0.1. (b) Remanence lost starting from 15 mT (AF of IRM and PRM not shown). Note that here we show the NRM removed up to only 85 mT, but we use data up to 225 mT to calculate the HC component (see Figure 2 and Table 1).

the LC component is apparently nonunidirectional in the four subsamples studied in Garrick-Bethell *et al.* [2009] (if the samples are rotated so that they have a common HC direction). In contrast, a PRM should produce unidirectional magnetization, since it would likely form in the presence of fields with longer length scales. We cannot completely rule out an SRM origin for the LC component but consider it highly unlikely.

For the sake of assessing whether 76535 records a dynamo field, it is much more important to consider whether the HC component may be due to a PRM. The HC component is unlikely to be the same putative PRM that may have caused the LC component because there is a marked difference in direction between the LC and HC components (Figure 4). Furthermore, it is also unlikely to be a different PRM because there is no measurable loss of the 1.8 GPa PRM above 25 mT and the PRM-experiment remanence returned to

Demagnetization of both ARM and NRM is fairly noisy due to spurious remanence acquisition.

3.3.3. Comparison of NRM With PRM and Possible Evidence for a Partial SRM

Sample 76535 may have been exposed to peak pressures as high as 5 GPa (constrained by petrologic observations) [Garrick-Bethell *et al.*, 2009; Gooley *et al.*, 1974]. We observe a roughly linear relationship between acquired PRM and pressure over the range of 0 and 1.8 GPa, as observed for other lunar samples [Shea *et al.*, 2012]. This linearity allows us to estimate the PRM acquired at the maximum allowable 5 GPa pressure which is inaccessible to our laboratory equipment (Figure 6).

We explore the possibility that the LC or HC components are SRMs. The similar slopes of remanence lost versus AF field for the LC component of the NRM and the PRM suggest the putative LC component could be a PRM (Figure 5a). The magnetization intensity of the LC component after VRM removal at AF 3.5 mT is $\sim 4.2 \times 10^{-9} \text{ Am}^2$ (Figure 5a). Using the measurements of AF of PRM at 3.0 mT (close to the VRM AF removal level), and extrapolating them to 5 GPa (Figure 6), we find that a paleo-field of $\approx 2000 \mu\text{T}$ is required to produce this remanence as a 5 GPa SRM. It is conceivable, but unlikely that such high paleofields could be produced in an impact-generated plasma [Crawford and Schultz, 1999; Hood and Artemieva, 2008; Oran *et al.*, 2016; Srnka, 1977]. Some evidence against the PRM interpretation is that

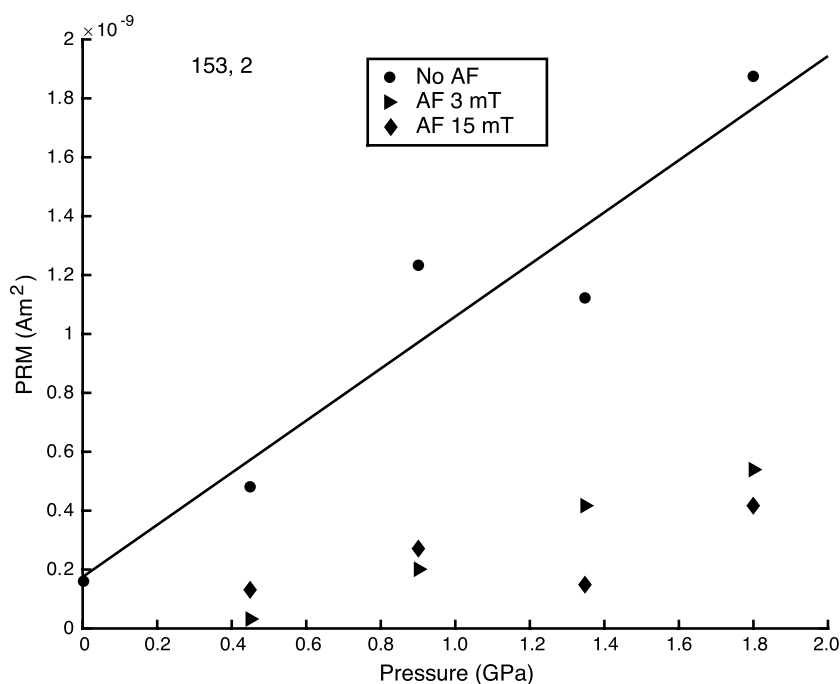


Figure 6. Total PRM acquired versus applied pressure (0, 0.45, 0.9, 1.35, and 1.8 GPa) for subsample 2 in a field of 0.8 mT (circles). The best fit line is also shown. AF demagnetization at 3 and 15 mT for each of the steps above 0 GPa is also shown (triangles and diamonds, respectively).

its pre-PRM value by AF demagnetization to only 23 mT. This suggests that the coercivity range affected by a PRM acquired in pressures even several times higher (≈ 5 GPa) is not likely to produce remanence in grains with coercivities up to at least 225 mT like those containing the HC component.

3.4. Paleointensity Estimates

To obtain a paleointensity estimate, we again focus on subsample 2 because it exhibits the clearest HC component. We find that its HC paleointensities are fairly consistent across different bias fields for the ARM method, ranging from 20 to $26 \pm 9 \mu\text{T}$ (95% confidence interval from regressions, Figure 7a and Table 3). The HC paleointensity from the IRM method is $40 \pm 10 \mu\text{T}$ (Figure 7b and Table 3). When corrected for anisotropy, these values change by $<3\%$. The implied LC component paleointensities are at least an order of magnitude larger (Table 3), which we interpret to be implausible for a dynamo field, and thus, they are consistent with their origin as an artificial IRM.

Previous ARM paleointensity experiments showed that AF methods are capable of retrieving paleointensities from subsample 2 for magnetizing fields $>3 \mu\text{T}$ [Tikoo *et al.*, 2012]. Below this field, the remanence is too weak to be resolved with AF demagnetization due to spurious ARM, GRM, and anisotropy effects. However, this $3 \mu\text{T}$ limit generously assumed that the component of interest was blocked starting from an AF level of 0 mT. Since the HC component actually starts at approximately 15 mT due to the IRM overprint, we reprocessed the paleointensity limit data of Tikoo *et al.* [2012] to exclude coercivities <15 mT. As a result, the minimum paleointensity fidelity limit increases to $\approx 15 \mu\text{T}$ (the value where the fractional difference between the applied and retrieved field increases markedly (Figure 8)). This limit indicates the inferred HC paleointensity of 20 – $40 \mu\text{T}$ is marginally resolvable, which explains the difficulty in measuring it here and in Garrick-Bethell *et al.* [2009].

3.5. $^{40}\text{Ar}/^{39}\text{Ar}$ and $^{38}\text{Ar}/^{37}\text{Ar}$ Thermochronology

The observed $^{40}\text{Ar}/^{39}\text{Ar}$ release spectra of both aliquots are in mutual agreement and show little evidence of open system behavior of radiogenic ^{40}Ar . The consistency in apparent Ca/K ratios indicates that Ar was primarily degassed from a single phase during the analyses (Figure 9). Nearly all extractions of each analysis plot are within analytical uncertainty of a well-defined plateau age of 4249 ± 7 Ma (one standard deviation analytical uncertainty; ± 12 Ma including decay constant and fluence monitor uncertainties), which is far more

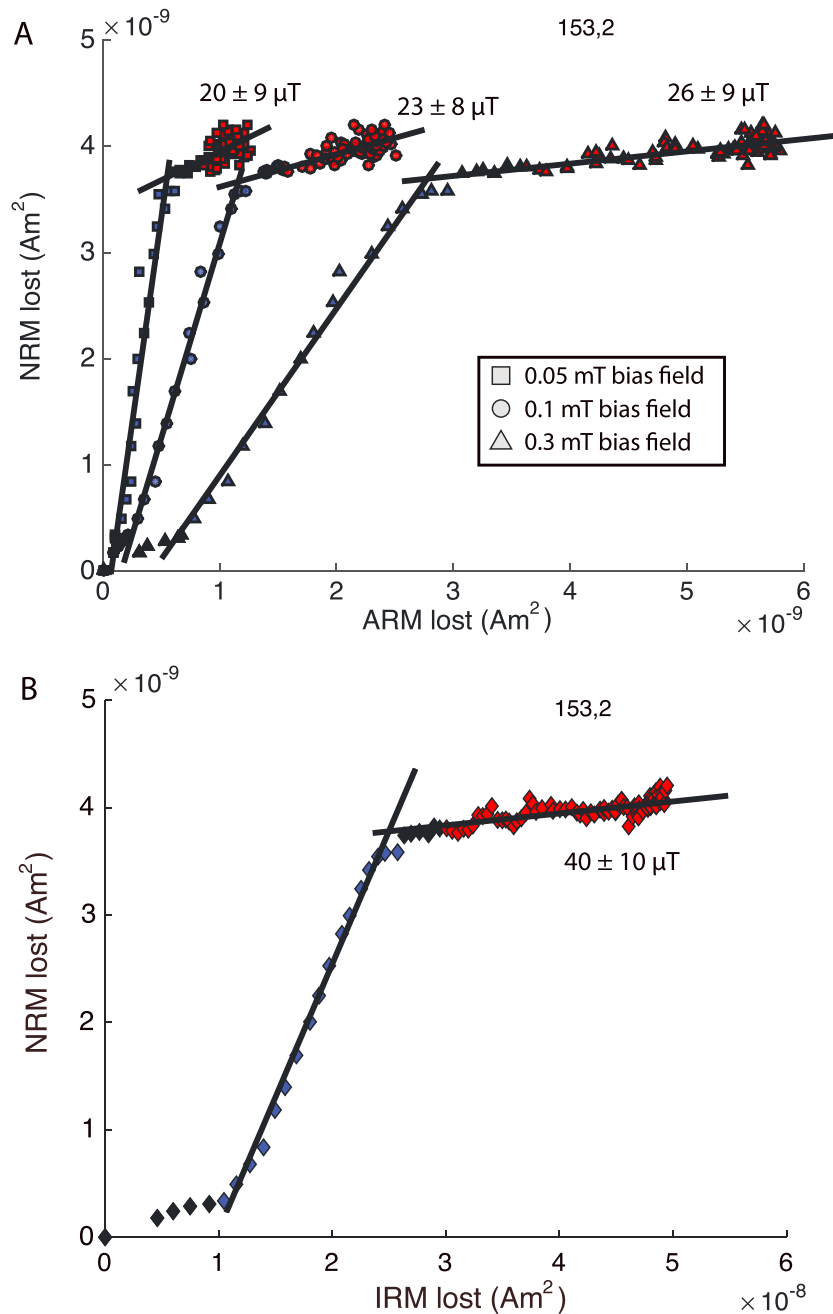


Figure 7. Paleointensity experiments for subsample 2. (a) NRM lost versus ARM lost, for the ARM bias fields shown (squares = 0.05 mT, circles = 0.1 mT, and triangles = 0.3 mT), acquired in a peak field of 250 mT. (b) NRM lost versus IRM lost for an IRM acquired in a field of 250 mT. The black lines in each figure show the best fit slope for the LC and HC components, over the AF ranges 3.5–11.5 mT and 15–85 mT, respectively. Black points are data not included in either fit (0–3.0 and 12.0–14.5 mT). Slopes and paleointensities are shown in Table 3, and HC paleointensities are shown on the figures. While the HC component was estimated using AF fields up to 225 mT, we only calculated the ARM and IRM lost up to 85 mT for the paleointensity experiment because this region has the least amount of ARM noise.

precise than the 4200–4300 Ma age inferred by *Husain and Schaeffer* [1975]. This age is very similar to the U-Pb age of 4.236 ± 15 Ma reported in *Premo et al.* [1992] and the $^{40}\text{Ar}/^{39}\text{Ar}$ age of 4.21–4.23 Ga reported by *Park et al.* [2015].

Assuming that cosmogenic ^{38}Ar is primarily derived from plagioclase with a production rate $P_{38\text{Ca}} = 8.081 \times 10^{-13}$ mol/gCa/Ma, we estimate the apparent cosmogenic ^{38}Ar exposure age of each step

Table 3. Slopes for the Paleointensity Experiments for the LC and HC Components for Subsample 2, Using the ARM and IRM Methods, Along With 95% Confidence Intervals (See Figure 7)^a

Measurement Type	LC Slope ^b	HC Slope ^c	HC Paleointensity (μT) ^c
ARM (0.05 mT)	4.2 ± 0.4	0.5 ± 0.2	20 ± 9
ARM (0.1 mT)	3.2 ± 0.1	0.3 ± 0.1	23 ± 8
ARM (0.3 mT)	1.6 ± 0.1	0.11 ± 0.04	26 ± 9
IRM (250 mT)	0.25 ± 0.01	0.013 ± 0.004	40 ± 10

^aThe inferred HC paleointensities using the equations in section 2 are also shown.^bAF steps 3.5–11.5 mT.^cAF steps 15.0–85.0 mT.

following the procedures described in *Cassata et al.* [2010] and *Shea et al.* [2012]. The mean cosmogenic ^{38}Ar ages calculated from all release steps of the two aliquots are 140.8 ± 12.7 and 142.3 ± 3.0 Ma (one standard deviation uncertainties, not including production rate uncertainty), with a weighted mean exposure age of 142 ± 3 Ma. This is slightly lower than the ~ 220 Ma exposure age reported by *Lugmair et al.* [1976].

Using models for the production and diffusion of Ar, and derived diffusion parameters [e.g., see *Fechtig and Kalbitzer* [1966], *Shuster et al.* [2010], *Suavet et al.* [2013], and supporting information Appendix A2), we are able to place bounds on the sample's thermal history at 142 Ma. Even for brief (<1 s long) heating events like those expected during an impact that likely brought 76535 to the surface by ≈ 142 Ma, the $^{40}\text{Ar}/^{39}\text{Ar}$ data require temperatures significantly below 400°C (Figures S3c and S3d). Using a similar model involving cosmogenic ^{38}Ar produced solely since surface exposure age [*Shea et al.*, 2012], the upper bound on surface heating over the last 142 Ma is $<170^\circ\text{C}$ (Figures S3a and S3d).

We can also assess how the sample may have been thermally affected by the late heavy bombardment at 3.9 Ga. At this time, it would have likely been at least 2 m deep to avoid undergoing cosmogenic ^{38}Ar production. Therefore, 2 m is a conservative lower limit on the thickness of any hot ejecta deposit that the sample was contained in or near. The conductive cooling time of a 2 m thick layer is ≈ 1 month (assuming thermal diffusivity $= 10^{-6} \text{ m}^2/\text{s}$). This timescale implies a maximum allowable temperature of $\approx 475^\circ\text{C}$ at 3.9 Ga (Figure S3d), well below the Curie temperature. A 100 m thick layer cools in ≈ 300 years, implying maximum temperatures of $\approx 375^\circ\text{C}$.

3.6. Cosmogenic Neon Thermochronology

Four of the five unirradiated anorthite grains we analyzed have Ne isotopic compositions that plot on a mixing line between cosmogenic and solar wind components (Figure S4 and Table S6). The fifth analysis (aliquot ν) plots below this mixing line, suggesting Ne isotope fractionation during solar wind implantation [*Grimberg et al.*, 2006] and is not used in thermal history calculations. We deconvolved the cosmogenic component from the solar wind component in the remaining four analyses (Table S6). Using the elemental production rates of cosmogenic neon in [*Leya et al.*, 2001] and the composition of 76535 anorthite from *Dymek et al.* [1975], we calculated the total cosmogenic abundance of each Ne isotope produced in these anorthite grains during the 142 ± 3 Ma exposure of 76535 (Table S6). Comparison of the observed cosmogenic Ne abundances to the total cosmogenic Ne produced during exposure indicates that between 8 and 67% of the cosmogenic Ne was diffusively lost (Table S6), with the amount of diffusive loss inversely correlated to the grain size analyzed.

Using the diffusion parameters calculated from the step degassing experiment (Figure S4), we modeled the simultaneous production and diffusion of cosmogenic neon in each anorthite grain for different effective diffusion temperatures (EDTs) [*Tremblay et al.*, 2014]. We find that a weighted mean EDT of $75.5 \pm 4.2^\circ\text{C}$ best predicts the observed cosmogenic neon abundances (Figure S4). This is in excellent agreement with the weighted mean EDT of $77.0 \pm 1.3^\circ\text{C}$ calculated from $^{40}\text{Ar}/^{39}\text{Ar}$ and $^{38}\text{Ar}/^{37}\text{Ar}$ whole rock measurements of Apollo 15 samples [*Shuster and Cassata*, 2015]. Given our calculated neon diffusion parameters and direct lunar surface temperature measurements [*Keihm and Langseth*, 1973], we estimate a modern EDT at the Apollo 17 landing site of $\sim 83^\circ\text{C}$ (Figure S5). Collectively, these results demonstrate that 76535 has only experienced heating due to insolation during its 142 Ma exposure at the lunar surface.

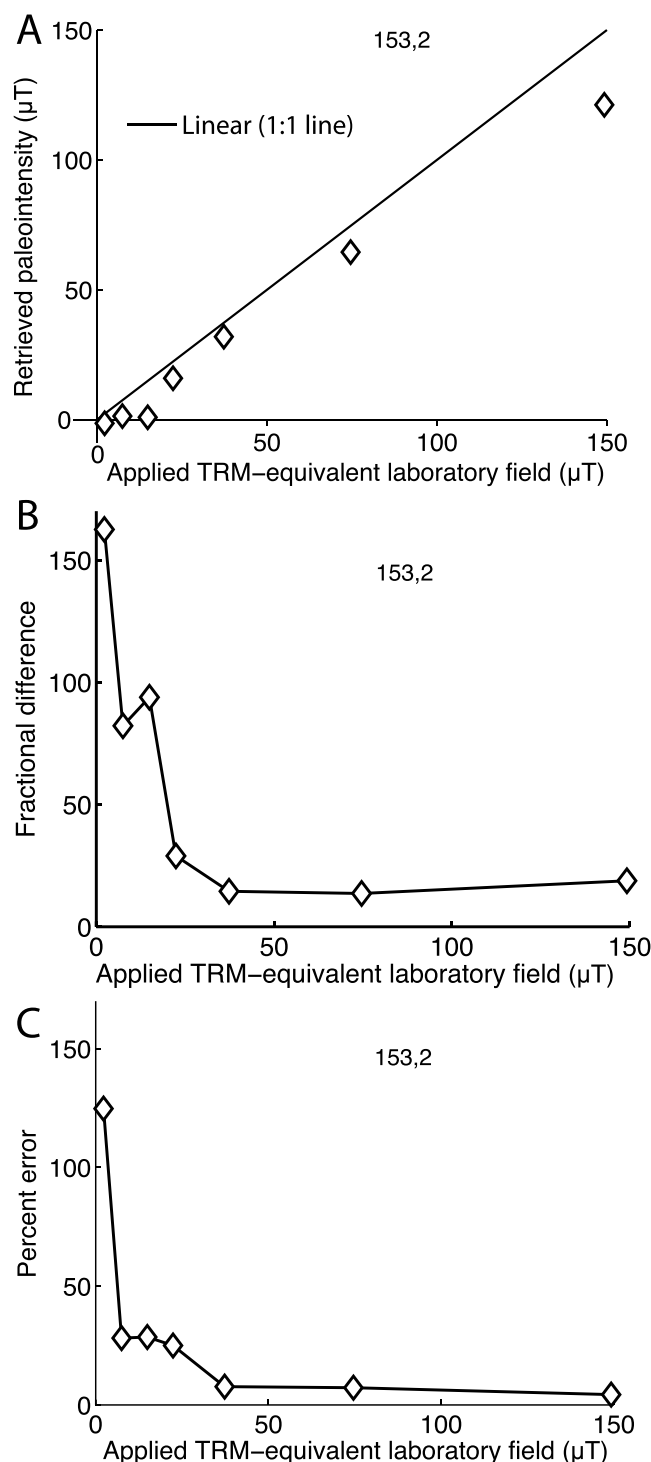


Figure 8. Paleointensity limit tests for subsample 2. (a) Retrieved paleointensities from the ARM lost method using laboratory ARM as a synthetic TRM and calculated for remanence lost from 15 mT. (b) Fractional difference between the applied field and the retrieved field in Figure 8a. (c) The percent difference between the calculated 95% confidence interval and the retrieved paleointensity (100% equals an uncertainty equal to the paleointensity).

4. Discussion and Interpretation

4.1. HC Component From an Early Dynamo Field

While the demagnetization behavior of 76535 is not ideal, five lines of evidence suggest that 76535 records an ancient dynamo field at 4.25 Ga. First, demagnetization of NRM behaves like that of a weak-bias-field ARM over the same AF coercivity range, and differently from IRM and PRM. Second, the HC component in subsample 2 decays to the origin, implying that this remanence represents the final component. Third, the paleointensity estimate for this component (20–40 μT) is higher than would be expected for long-lived non-dynamo fields such as the interplanetary magnetic field and crustal magnetic fields [Fuller and Cisowski, 1987]. Fourth, the rock has not experienced significant reheating events after 4.25 Ga. Finally, and most importantly, the HC components in all subsamples have nearly indistinguishable directions (all directions plus their MAD angles overlap, Figure 4).

It is difficult to imagine an alternative to the lunar dynamo hypothesis that would lead to a HC component in the same direction in three different subsamples. This common direction cannot be from magnetic anisotropy because the samples do not have common principal anisotropy axis directions. Furthermore, previous studies of the petrography of 76535 have not reported any observed foliations or fabrics at the >1 mm scale [Dymek et al., 1975; Gooley et al., 1974]. Any instrument bias can also be ruled out by the fact that subsample 1 was measured inverted relative to the others (section 2 and 3.1.1).

Our paleointensity estimate of 20–40 μT is roughly consistent with the upper bound of the field estimates for impact stirred dynamos ($\sim 20 \mu\text{T}$) and higher than the upper estimate of $\sim 12 \mu\text{T}$ for Earth-like

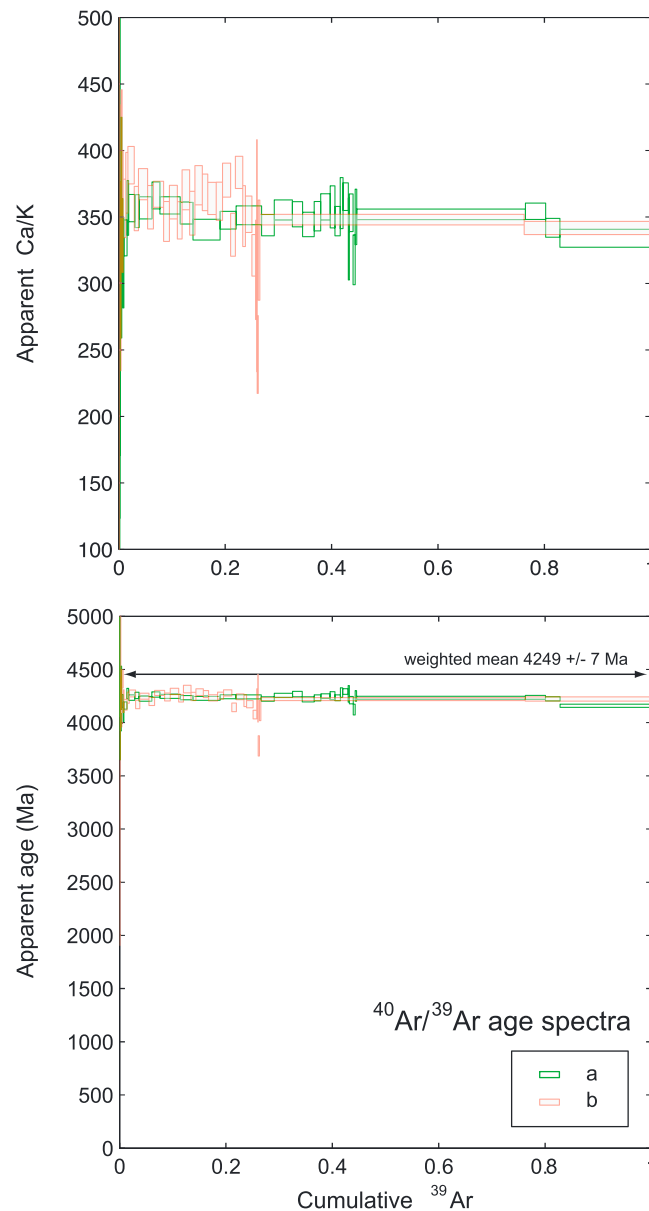


Figure 9. Whole rock $^{40}\text{Ar}/^{39}\text{Ar}$ geochronology of 76535. The bottom panel shows the apparent $^{40}\text{Ar}/^{39}\text{Ar}$ ages calculated for each degassing step of two aliquots of 76535 calculated from data in Table S4 plotted against the cumulative release fraction of ^{39}Ar . The weighted mean plateau age calculated from both analyses is 4249 ± 7 Ma. The top panel shows the apparent Ca/K ratios for each analysis.

there may be remanence carriers at higher coercivities than accessible with our AF demagnetization equipment (limited to 290 mT).

4.2. MC Component Interpretation

While the HC component supports the previous conclusion of a dynamo field on the Moon at 4.25 Ga, Garrick-Bethell *et al.* [2009] also previously identified an additional MC component of magnetization, separated from the HC component by $\approx 146^\circ$, across four subsamples. In their study, sample 76535,138,2 was mutually oriented with respect to sample 76535,138,3 (section 1), but 138,3 also did not have an easily identifiable MC component. Why do we not observe a definitive MC component in this study and sample 138,3 in the previous study? We offer three possible explanations.

convection-driven dynamos [Weiss and Tikoo, 2014]. Our paleointensity is higher than the lowermost limit of $0.3 \mu\text{T}$ in Garrick-Bethell *et al.* [2009] (but close to the nominal values they reported: $25\text{--}66 \mu\text{T}$), because they used an extreme range of calibration factors a and f in their paleointensity calculations (equation (1)). Unfortunately, the calibration factors for a lithology like troctolite 76535 have not been well determined. Until experiments are done relating TRM to IRM and ARM for 76535, uncertainty will remain in the absolute paleointensity. As discussed in section 2.1, the two-standard-deviation uncertainty is estimated to be a factor of 2–3 [Weiss and Tikoo, 2014]. If our paleointensity was a factor of 3 too high, the lower end of our estimate would be $\sim 7 \mu\text{T}$.

An important observation we must explain is why three subsamples have a unidirectional HC component, but only subsample 2 unequivocally decays to the origin. We suggest three possible explanations. The first is that spurious ARM acquired during AF demagnetization obscures decay of the NRM during demagnetization. This effect has been observed in other lunar samples [Fuller and Cisowski, 1987; Tikoo *et al.*, 2012] and metal-bearing meteorites [Weiss *et al.*, 2010b]. It is particularly important for samples like 76535 whose paleointensities ($20\text{--}40 \mu\text{T}$) are close to their paleointensity fidelity limits ($\approx 15 \mu\text{T}$; section 3.4). The second explanation is that GRM may not have been completely removed by the averaging method [Hu *et al.*, 1998]. The third explanation is that given that single-domain iron crystals can have microcoercivities up to $\approx 1 \text{ T}$ [Dunlop and Özdemir, 1997],

Table 4. Distance From the HC to LC Components in This Study and Garrick-Bethell *et al.* [2009]^a

Subsample Number	Angular Distance Between HC and LC (°)
<i>This Study</i>	
153,1	62.0
153,2	48.2
153,3	44.2
	Mean = 51.5°, $\sigma = 9.3^\circ$
<i>Previous Study</i>	
137,1	105.8
137,7	118.8
137,8	86.7
138,2	35.1
	Mean = 86.6°, $\sigma = 36.8^\circ$

^aHC directions are corrected for anisotropy, while LC components are not.

The first is that, as discussed for the HC component (section 4.1), the MC component may be difficult to resolve due to the marginal magnetic recording properties of the subsamples relative to paleointensity recorded. For example, in the supporting information Appendix A1, we show that subsample 1 is capable of recording a clear MC component only up to ≈ 23 mT, and between 15 and 145 mT its NRM stays away from the HC direction, which may be due to a MC component that is difficult to resolve.

The second explanation is that overlapping coercivity distributions may cause any putative MC component to appear close to the HC component (supporting information Appendix A1).

Related to this is the possibility of nonuniform coercivity distributions that differ amongst the subsamples, such that some samples have few remanence carrying grains in the MC range. For example, subsample 1 shows little change in direction between removal of the LC component at 15 mT and the final demagnetization direction, while sample 76535, 137,7 in the previous study shows a large change in direction by 27.6 mT, subsequent removal of the MC component, and then decay to the origin [Garrick-Bethell *et al.*, 2009, Figure 1].

The third possibility is that the MC component inferred in the previous study is simply a laboratory artifact of spurious ARM and GRM during AF demagnetization. In this case, the coincidence of the $\approx 146^\circ$ distances between the MC and HC components in the four samples previously studied would be by chance and the clustering of the remanence over 15–145 mT in subsample 1 in the present study could be a poorly characterized effect of anisotropy or spurious ARM. However, the odds of four directions randomly clustering at a distance of 145.6° (the mean distance), over an angular interval equal their mean uncertainty of 21° , is only 3% (assuming the HC direction is fixed at a pole, and the MC distances from it are randomly distributed). At any rate, even if the clustering was by chance, it would not affect our interpretation of the HC component.

Relevant to the third possibility is that a new interpretation of the rock's thermal history suggests that only one TRM component (such as HC) may be required, in contrast to the two MC and HC components previously inferred. Garrick-Bethell *et al.* [2009] inferred that the rock cooled in the deep crust (≈ 45 km) and was reheated to $\approx 600^\circ\text{C}$ when it was excavated and buried in an ejecta blanket for ≈ 10 kyr. Because 600°C is lower than the inferred Curie temperature of $\approx 850^\circ\text{C}$, Garrick-Bethell *et al.* [2009] inferred the rock acquired an HC component in the deep crust and a second MC component in the ejecta blanket. The 600°C temperature used in their study was based on the metamorphism temperature of the anorthite $\bar{I}\bar{T} \rightarrow P\bar{T}$ symmetry transition reported by Nord [1976]. However, the transition temperature for 95% molar anorthite was actually subsequently revised upward by Grove *et al.* [1983] to 700 – 1000°C . These higher temperatures span the 780 – 850°C Curie point of 76535 [Garrick-Bethell *et al.*, 2009]. Therefore, if the transition takes place at the higher end of this range, 76535 would have been totally remagnetized during cooling in the hot ejecta blanket, implying the existence of only one (HC) lunar magnetization component dating to the ejection event at 4.25 Ga.

4.3. LC Component Interpretation

Previously, Garrick-Bethell *et al.* [2009] also reported that the LC directions were different across four different subsamples, when all subsamples were referenced to a frame that shared the same HC direction (Table 4). However, the LC components in the three subsamples in this study are nearly unidirectional (Table 4). As discussed in section 3.3.3, a plausible solution to this apparent inconsistency is that the IRM field was curved on the scale of the rock (≈ 5 cm), but not on the scale of the subsample we used here (unfortunately the distance from the sample studied here to the samples in Garrick-Bethell *et al.* [2009] is unknown). If true, this would also help rule out a PRM origin for the LC component. This interpretation is also consistent with observations of weak nonunidirectional IRMs inferred to be present in other lunar and meteorite samples [Weiss *et al.*, 2010a]. Finally, this interpretation is also supported by the nearly equal

directions of the two LC components of the simpler two-piece mutual-orientation study of samples 76535,138,2 and 76535,138,3 in Garrick-Bethell *et al.* [2009].

5. Conclusions

The demagnetization behavior of 76535 is nonideal, and the MC component in the previously studied samples was difficult to identify in this study. However, the common direction of the HC component in all three subsamples (Figure 4) strongly suggests a temporally stable field on the Moon at the newly defined $^{40}\text{Ar}/^{39}\text{Ar}$ plateau age of 4249 ± 12 Ma. This implies a dynamo with a surface field strength of tens of microteslas was present on the Moon at this time. Such a dynamo could have been generated by one of several mechanisms: (1) a thermal or chemical convection dynamo lasting from the time of Moon formation, assuming a mantle that is either dry (operating until at least 4.1 Ga) [Konrad and Spohn, 1997; Laneuville *et al.*, 2014; Stegman *et al.*, 2003] or wet (operating as late as 2.5 Ga) [Evans *et al.*, 2014], (2) a late onset dynamo driven by delayed upwelling of a cumulate layer at the core-mantle boundary [Stegman *et al.*, 2003; Zhang *et al.*, 2013], or (3) a mechanically stirred dynamo from precession or impacts [Dwyer *et al.*, 2011; Le Bars *et al.*, 2011]. The first case is plausible since the revised $^{40}\text{Ar}/^{39}\text{Ar}$ age is ≈ 150 Ma older than the earliest time of dynamo cessation. The second case is marginally rejected by our results. For example, both Stegman *et al.* [2003] and Zhang *et al.* [2013] suggest that a dynamo would have been delayed until ≈ 250 Ma after magma ocean crystallization, or at ≈ 4.2 – 4.1 Ga, assuming magma ocean overturn was completed by ≈ 4.47 – 4.32 Ga [Elkins-Tanton, 2012]. This range nearly excludes the 4249 Ma age of the NRM in 76535. Zhang *et al.* [2013] further suggest that the dynamo should coincide with the onset of mare volcanism (>4.0 Ga). For the third case, both precession-driven and impact-generated dynamos are plausible at 4249 Ma. Therefore, it is not presently possible to rule conclusively for either the first or third mechanism.

Acknowledgments

This work was supported by the BK21 plus program through the National Research Foundation (NRF) funded by the Ministry of Education of Korea. I.G.B. and B.P.W. acknowledge support from the NASA Solar System Exploration and Research Virtual Institute node at Brown-MIT and the NASA Solar System Workings program (grants NNX15AL62G and NNX15AH47G). G.B. acknowledges support from the Alfred P. Sloan Foundation. D.L.S. and M.M.T. acknowledge support from the NSF Petrology and Geochemistry Program (EAR-1322086). We are grateful to CAPTEM and the Johnson Space Center staff in allocating and processing sample 76535. We thank Jérôme Gattacceca for loaning us his high-pressure loading cell. S.M.T. was supported by a NASA Earth and Space Science Fellowship; S. M.T. and M.M.T. were supported by NSF Graduate Research Fellowships. AF demagnetization data and thermochronology data are included in the supporting information.

References

- Arkani-Hamed, J., and D. Boutin (2014), Analysis of isolated magnetic anomalies and magnetic signatures of impact craters: Evidence for a core dynamo in the early history of the Moon, *Icarus*, **237**, 262–277.
- Bezaeva, N. S., J. Gattacceca, P. Rochette, R. A. Sadykov, and V. I. Trukhin (2010), Demagnetization of terrestrial and extraterrestrial rocks under hydrostatic pressure up to 1.2 GPa, *Phys. Earth Planet. Inter.*, **179**, 7–20.
- Bogard, D. D., L. E. Nyquist, B. M. Bansal, H. Wiesmann, and C. Y. Chih (1975), 76535: An old lunar rock, *Earth Planet. Sci. Lett.*, **26**, 69–80.
- Cassata, W. S., P. R. Renne, and D. L. Shuster (2009), Argon diffusion in plagioclase and implications for thermochronometry: A case study from the Bushveld Complex, South Africa, *Geochim. Cosmochim. Acta*, **73**, 6600–6612.
- Cassata, W. S., D. L. Shuster, P. R. Renne, and B. P. Weiss (2010), Evidence for shock heating and constraints on Martian surface temperatures revealed by $^{40}\text{Ar}/^{39}\text{Ar}$ thermochronometry of Martian meteorites, *Geochim. Cosmochim. Acta*, **74**, 6900–6920.
- Cisowski, S. M., D. W. Collinson, S. K. Runcorn, A. Stephenson, and M. Fuller (1983), A review of lunar paleointensity data and implications for the origin of lunar magnetism, in *Proceedings of the 13th Lunar and Planetary Science Conference*, pp. A691–A704, AGU, Houston, Tex.
- Cournède, C., J. Gattacceca, and P. Rochette (2012), Magnetic study of large Apollo samples: Possible evidence for an ancient centered dipolar field on the Moon, *Earth Planet. Sci. Lett.*, **331**, 31–42.
- Crawford, D. A., and P. H. Schultz (1999), Electromagnetic properties of impact-generated plasma, vapor and debris, *Int. J. Impact Eng.*, **23**, 169–180.
- Dunlop, D. J., and Ö. Özdemir (1997), *Rock Magnetism: Fundamentals and Frontiers*, 596 pp., Cambridge Univ. Press, Cambridge, U. K.
- Dwyer, C. A., D. J. Stevenson, and F. Nimmo (2011), A long-lived lunar dynamo driven by continuous mechanical stirring, *Nature*, **479**, 212–214.
- Dymek, R. F., A. L. Albee, and A. A. Chodos (1975), Comparative petrology of lunar cumulate rocks of possible primary origin—Dunite 72415, troctolite 76535, norite 78235, and anorthosite 62237, in *Proceedings of the 6th Lunar and Planetary Science Conference*, pp. 301–341, Pergamon Press, Houston, Tex.
- Elkins-Tanton, L. T. (2012), Magma oceans in the inner solar system, *Annu. Rev. Earth Planet. Sci.*, **40**, 113–139.
- Evans, A. J., M. T. Zuber, B. P. Weiss, and S. M. Tikoo (2014), A wet, heterogeneous lunar interior: Lower mantle and core dynamo evolution, *J. Geophys. Res. Planets*, **119**, 1061–1077, doi:10.1002/2013JE004494.
- Fechtig, H., and S. T. Kalbitzer (1966), The diffusion of argon in potassium-bearing solids, in *Potassium Argon Dating*, edited by O. A. Schaeffer and J. J. Zahring, pp. 68–107, Springer, New York.
- Fu, R. R., B. P. Weiss, D. L. Shuster, J. Gattacceca, T. L. Grove, C. Suavet, E. A. Lima, L. Li, and A. T. Kuan (2012), An ancient core dynamo in Asteroid Vesta, *Science*, **338**, 238–241.
- Fuller, M., and S. M. Cisowski (1987), Lunar paleomagnetism, in *Geomagnetism*, vol. 2, edited by J. A. Jacobs, pp. 307–455, Academic Press, New York.
- Garrick-Bethell, I., and B. P. Weiss (2010), Kamacite blocking temperatures and applications to lunar magnetism, *Earth Planet. Sci. Lett.*, **294**(1–2), 1–7, doi:10.1016/j.epsl.2010.02.013.
- Garrick-Bethell, I., B. P. Weiss, D. L. Shuster, and J. Buz (2009), Early lunar magnetism, *Science*, **323**(5912), 356–359, doi:10.1126/science.1166804.
- Gattacceca, J., and P. Rochette (2004), Toward a robust normalized magnetic paleointensity method applied to meteorites, *Earth Planet. Sci. Lett.*, **227**, 377–393.
- Gooley, R., R. Brett, J. Warner, and J. R. Smyth (1974), A lunar rock of deep crustal origin: Sample 76535, *Geochim. Cosmochim. Acta*, **38**, 1329.
- Grimberg, A., H. Baur, P. Bochsler, F. Bühler, D. S. Burnett, C. C. Hays, V. S. Heber, A. J. G. Jurewicz, and R. Wieler (2006), Solar wind neon from Genesis: Implications for the lunar noble gas record, *Science*, **314**, 1133–1135.

- Grove, T. L., J. M. Ferry, and F. S. Spear (1983), Phase transitions and decomposition relations in calcic plagioclase, *Am. Mineral.*, **68**, 41–59.
- Halekas, J. S., R. P. Lin, and D. L. Mitchell (2003), Magnetic fields of lunar multi-ring impact basins, *Meteorit. Planet. Sci.*, **38**, 565–578.
- Hood, L. L., and N. A. Artemieva (2008), Antipodal effects of lunar basin-forming impacts: Initial 3D simulations and comparisons with observations, *Icarus*, **193**, 485–502.
- Hood, L. L., N. C. Richmond, and P. D. Spudis (2013), Origin of strong lunar magnetic anomalies: Further mapping and examinations of LROC imagery in regions antipodal to young large impact basins, *J. Geophys. Res. Planets*, **118**, 1265–1284, doi:10.1002/jgre.20078.
- Hu, S., E. Appel, V. Hoffmann, W. W. Schmahl, and S. Wang (1998), Gyromagnetic remanence acquired by greigite (Fe₃S₄) during static three-axis alternating field demagnetization, *Geophys. J. Int.*, **134**, 831–842.
- Huneke, J. C., and G. J. Wasserburg (1975), Trapped ⁴⁰Ar in troctolite 76535 and evidence for enhanced ⁴⁰Ar–³⁹Ar age plateaus, in *6th Lunar and Planetary Science Conference Abstracts*, pp. 417–419, Lunar and Planetary Institute, Houston, Tex.
- Husain, L., and O. A. Schaeffer (1975), Lunar evolution—The first 600 million years, *Geophys. Res. Lett.*, **2**, 29–32, doi:10.1029/GL002i001p00029.
- Jelinek, V. (1981), Characterization of the magnetic fabric of rocks, *Tectonophysics*, **79**, 63–67.
- Keilm, S. J., and M. G. Langseth Jr. (1973), Surface brightness temperatures at the Apollo 17 heat flow site: Thermal conductivity of the upper 15 cm of regolith, in *Proceedings of the 4th Lunar and Planetary Science Conference*, pp. 2503–2513, Houston, Tex.
- Kirschvink, J. L. (1980), The least-squares line and plane and the analysis of paleomagnetic data: Examples from Siberia and Morocco, *Geophys. J. R. Astron. Soc.*, **62**, 699–718.
- Konrad, W., and T. Spohn (1997), Thermal history of the moon—Implications for an early core dynamo and post-accretionary magmatism, *Adv. Space Res.*, **19**, 1511–1521.
- Laneuville, M., M. A. Wieczorek, D. Breuer, and N. Tosi (2013), Asymmetric thermal evolution of the Moon, *J. Geophys. Res. Planets*, **118**, 1435–1452, doi:10.1002/jgre.20103.
- Laneuville, M., M. A. Wieczorek, D. Breuer, J. Aubert, G. Morard, and T. Rückriemen (2014), A long-lived lunar dynamo powered by core crystallization, *Earth Planet. Sci. Lett.*, **401**, 251–260.
- Lawrence, K., C. Johnson, L. Tauxe, and J. Gee (2008), Lunar paleointensity measurements: Implications for lunar magnetic evolution, *Phys. Earth Planet. Inter.*, **168**, 71–87.
- Le Bars, M., M. A. Wieczorek, Ö. Karatekin, D. Cébron, and M. Laneuville (2011), An impact-driven dynamo for the early Moon, *Nature*, **479**, 215–218.
- Leya, I., S. Neumann, R. Wieler, and R. Michel (2001), The production of cosmogenic nuclides by GCR-particles for 2 pi exposure geometries, *Meteorit. Planet. Sci.*, **36**, 1547–1561.
- Lugmair, G. W., K. Marti, J. P. Kurtz, and N. B. Scheinin (1976), History and genesis of lunar troctolite 76535 or: How old is old, in *Lunar and Planetary Science Conference Proceedings*, edited by R. B. Merrill, pp. 2009–2033.
- McCallum, I. S., and J. M. Schwartz (2001), Lunar MG suite: Thermobarometry and petrogenesis of parental magmas, *J. Geophys. Res.*, **106**, 27,969–27,983, doi:10.1029/2000JE001397.
- Meyer, J., and J. Wisdom (2011), Precession of the lunar core, *Icarus*, **211**, 921–924.
- Mitra, R., L. Tauxe, and J. S. Gee (2011), Detecting uniaxial single domain grains with a modified IRM technique, *Geophys. J. Int.*, **187**, 1250–1258.
- Nagata, T. (1961), *Rock Magnetism*, 350 pp., Maruzen Co., Tokyo.
- Nord, G. L., Jr. (1976), 76535—Thermal history deduced from pyroxene precipitation in anorthite, in *Proceedings of the 7th Lunar and Planetary Science Conference Proceedings*, edited by R. B. Merrill, pp. 1875–1888, Pergamon Press, Houston, Tex.
- Oran, R., Y. Shprits, and B. P. Weiss (2016), Can impact-amplified magnetic fields be responsible for magnetization on the Moon?, in *47th Lunar and Planetary Science Conference Abstracts*, Lunar and Planetary Institute, Houston, Tex., Abstract 3057.
- Park, J., L. E. Nyquist, G. F. Herzog, B. D. Turrin, F. N. Lindsay, J. S. Delaney, C. C. Swisher, C.-Y. Shih, and A. Yamaguchi (2015), Newly determined Ar/Ar ages of lunar troctolite 76535, in *46th Lunar and Planetary Science Conference Abstracts*, Lunar and Planetary Institute, Houston, Tex., Abstract 2018.
- Premo, W. R., M. Tatsumoto, and V. L. Sharpton (1992), U-Th-Pb, Rb-Sr, and Sm-Nd isotopic systematics of lunar troctolitic cumulate 76535—Implications on the age and origin of this early lunar, deep-seated cumulate, in *Proceedings of the 22nd Lunar and Planetary Science Conference*, pp. 381–397, Lunar and Planetary Institute, Houston, Tex.
- Renne, P. R., R. Mundil, G. Balco, K. Min, and K. R. Ludwig (2010), Joint determination of 40 K decay constants and ⁴⁰Ar*/⁴⁰K for the Fish Canyon sanidine standard, and improved accuracy for ⁴⁰Ar/³⁹Ar geochronology, *Geochim. Cosmochim. Acta*, **74**, 5349–5367.
- Renne, P. R., G. Balco, K. R. Ludwig, R. Mundil, and K. Min (2011), Response to the comment by W.H. Schwarz et al. on “Joint determination of 40 K decay constants and ⁴⁰Ar*/⁴⁰K for the Fish Canyon sanidine standard, and improved accuracy for ⁴⁰Ar/³⁹Ar geochronology” by P.R. Renne et al. (2010), *Geochim. Cosmochim. Acta*, **75**, 5097–5100.
- Sadykov, R. A., N. S. Bezaeva, A. I. Kharkovskiy, P. Rochette, J. Gattacceca, and V. I. Trukhin (2008), Nonmagnetic high pressure cell for magnetic remanence measurements up to 1.5 GPa in a superconducting quantum interference device magnetometer, *Rev. Sci. Instrum.*, **79**, 115102.
- Scheinberg, A., K. M. Soderlund, and G. Schubert (2015), Magnetic field generation in the lunar core: The role of inner core growth, *Icarus*, **254**, 62–71.
- Shea, E. K., B. P. Weiss, W. S. Cassata, D. L. Shuster, S. M. Tikoo, J. Gattacceca, T. L. Grove, and M. D. Fuller (2012), A long-lived lunar core dynamo, *Science*, **335**, 453.
- Shuster, D. L., and W. S. Cassata (2015), Paleotemperatures at the lunar surfaces from open system behavior of cosmogenic ³⁸Ar and radiogenic ⁴⁰Ar, *Geochim. Cosmochim. Acta*, **155**, 154–171.
- Shuster, D. L., G. Balco, W. S. Cassata, V. A. Fernandes, I. Garrick-Bethell, and B. P. Weiss (2010), A record of impacts preserved in the lunar regolith, *Earth Planet. Sci. Lett.*, **290**(1–2), 155–165, doi:10.1016/j.epsl.2009.12.016.
- Srnka, L. J. (1977), Spontaneous magnetic field generation in hypervelocity impacts, in *Proceedings of the 8th Lunar and Planetary Science Conference*, pp. 785–792, Pergamon Press, Houston, Tex.
- Stegman, D. R., M. A. Jelinek, S. A. Zatman, J. R. Baumgardner, and M. A. Richards (2003), An early lunar core dynamo driven by thermochemical mantle convection, *Nature*, **421**, 143–146.
- Steiger, R. H., and E. Jager (1977), Subcommittee on geochronology: Convention on the use of decay constants in geo- and cosmochronology, *Earth Planet. Sci. Lett.*, **36**, 359–362.
- Stephenson, A. (1993), Three-axis static alternating field demagnetization of rocks and the identification of natural remanent magnetization, gyroremanent magnetization, and anisotropy, *J. Geophys. Res.*, **98**, 373–381, doi:10.1029/92JB01849.

- Stephenson, A., and D. W. Collinson (1974), Lunar magnetic field paleointensities determined by an anhysteretic remanent magnetization, *Earth Planet. Sci. Lett.*, **23**, 220–228.
- Suavet, C., B. P. Weiss, W. S. Cassata, D. L. Shuster, J. Gattacceca, L. Chan, I. Garrick-Bethell, J. W. Head, T. L. Grove, and M. D. Fuller (2013), Persistence and origin of the lunar core dynamo, *Proc. Natl. Acad. Sci. U.S.A.*, **110**, 8453–8458.
- Takahashi, F., H. Tsunakawa, H. Shimizu, H. Shibuya, and M. Matsushima (2014), Reorientation of the early lunar pole, *Nat. Geosci.*, **7**, 409–412.
- Tauxe, L., and H. Staudigel (2004), Strength of the geomagnetic field in the Cretaceous Normal Superchron: New data from submarine basaltic glass of the Troodos Ophiolite, *Geochim. Geophys. Geosyst.*, **5**, Q02H06, doi:10.1029/2003GC000635.
- Tikoo, S. M., B. P. Weiss, J. Buz, E. A. Lima, E. K. Shea, G. Melo, and T. L. Grove (2012), Magnetic fidelity of lunar samples and implications for an ancient core dynamo, *Earth Planet. Sci. Lett.*, **337**, 93–103.
- Tikoo, S. M., B. P. Weiss, W. S. Cassata, D. L. Shuster, J. Gattacceca, E. A. Lima, C. Suavet, F. Nimmo, and M. D. Fuller (2014), Decline of the lunar core dynamo, *Earth Planet. Sci. Lett.*, **404**, 89–97.
- Tremblay, M. M., D. L. Shuster, and G. Balco (2014), Diffusion kinetics of ^3He and ^{21}Ne in quartz and implications for cosmogenic noble gas paleothermometry, *Geochim. Cosmochim. Acta*, **142**, 186–204.
- Weiss, B. P., and S. M. Tikoo (2014), The lunar dynamo, *Science*, **346**, 1198.
- Weiss, B. P., J. Gattacceca, S. Stanley, P. Rochette, and U. R. Christensen (2010a), Paleomagnetic records of meteorites and early planetesimal differentiation, *Space Sci. Rev.*, **152**, 341–390.
- Weiss, B. P., S. Pedersen, I. Garrick-Bethell, S. T. Stewart, K. L. Louzada, A. C. Maloof, and N. L. Swanson-Hysell (2010b), Paleomagnetism of impact spherules from Lonar crater, India and a test for impact-generated fields, *Earth Planet. Sci. Lett.*, **298**(1–2), 66–76, doi:10.1016/j.epsl.2010.07.028.
- Zhang, N., E. M. Parmentier, and Y. Liang (2013), A 3-D numerical study of the thermal evolution of the Moon after cumulate mantle overturn: The importance of rheology and core solidification, *J. Geophys. Res. Planets*, **118**, 1789–1804, doi:10.1002/jgre.20121.

Supporting Information for:

Further evidence for early lunar magnetism from troctolite 76535

I. Garrick-Bethell, B. P. Weiss, D. L. Shuster, S. M. Tikoo, and M. M. Tremblay

This file includes:

Appendix A1 - Possible MC component in subsample 1

Appendix A2 - Argon thermochronometry methods

Appendix A3 - Cosmogenic neon thermochronology methods

Appendix A1

Possible MC component in subsample 1

A difficulty in resolving two TRM components with AF demagnetization is that the coercivity distributions of each component may overlap. Such overlapping distributions could partially account for the difficulty in resolving an MC component in this study. In subsample 1, the clustered magnetization directions in the 15-145 mT range and remanence motion over an approximate great circle 145 to 175 mT suggest that there is either remanence near the cluster direction or that the anisotropy and spurious ARM are deflecting the magnetization toward this direction in addition to controlling the zig-zag behavior (as also observed for some mare basalts [Tikoo *et al.*, 2012]). Possible evidence favoring the latter is that the magnetization follows the anisotropy intermediate-easy plane up to ≈ 15 mT (Fig. 2d). To assess these two hypotheses further, we demagnetized a simulated two-component NRM with the goal of determining if the remanence is deflected towards the easy axis or easy plane during demagnetization. In particular, we simulated a HC and a possible MC component by applying ARMs with bias fields of 20 μ T and peak AC fields of 290 mT and 100 mT, respectively. The first component, labeled ARM1, was applied in the approximate direction of the HC component, and was followed by the second component, labeled ARM2, in the direction of the putative MC component (Fig. S1).

When the combined ARM1 and ARM2 magnetization is demagnetized, the remanence shows clear decay up to AF levels of 15 mT as the ARM2 component is removed (Fig. S1b). However, above 15 mT, little decay is observed and by 23 mT, the remanence exhibits zig-zag behavior very similar to that of the NRM (compare Fig. 2a, d and Fig. S1). During the zig-zagging, the magnetization directions cluster in an area approximately along the great circle that joins the ARM1 and ARM2 components. If we interpret this clustering to be the result of weak remanence being removed from the combined ARM1 and ARM2, it would imply that the similar clustering in the NRM may be due to an unresolved MC component towards the direction of the 15-145 mT cluster. However, the lack of clear decay of ARM2 above 23 mT also illustrates why it may be difficult to resolve such a component in this subsample.

The meaning of the previous experiment is somewhat ambiguous because the anisotropy easy axis happens to lie in the vicinity of the putative MC component direction. To address this, we conducted a second experiment to test whether subsample 1 exhibits zig-zag behavior in the absence of a remanence in the MC direction. We

applied a single-component ARM in the HC direction (this time with a slightly weaker bias field of 10 μ T), plus a 13-mT IRM in the direction of the LC component (to simulate the weak IRM overprint on natural samples) (Fig S2). When this combination of ARM and IRM was AF demagnetized, the remanence moved immediately towards the ARM direction after removal of the IRM and then moved towards a tight cluster near the original HC direction by 30 mT (Fig. S2, compare with Fig. 2d). Little or no zig-zag behavior is observed. This suggests that after demagnetization of the ARM, the magnetization direction returned to that of the undemagnetized HC remanence. The fact that the demagnetization of this simulated HC component did not deviate toward the putative MC/ARM2 direction and did not exhibit the same zig-zag motion supports the hypothesis that a real MC component exists in the NRM and controls the 15-145 mT clustering. However, the lack of an unambiguous isolation of an MC component makes this provisional.

Appendix A2

Argon thermochronometry methods

To place thermal constraints on the sample, we calculated apparent diffusion coefficients for both ^{39}Ar and ^{37}Ar extracted during each analysis following *Fechtig and Lakbitzer*, [1966] and procedures described in *Cassata et al.* [2010] and *Shea et al.* [2012]. This calculation requires that the total content of ^{39}Ar and ^{37}Ar are known. However, since the final extractions at $\sim 1400^\circ\text{C}$ yielded Ar in significant excess of the analytical blank abundance, we cannot demonstrate that the Ar was completely extracted from each aliquot, and must assume the total abundances. Based on the analysis of *Husain and Schaeffer* [1975], who heated an aliquot of 76535 to higher extraction temperatures (1700°C), we conservatively estimate that the observed ^{39}Ar and ^{37}Ar in all extractions up to 1400°C in our analyses amount to $\geq 25\%$ of that initially present in each sample. To incorporate uncertainty in this estimate, we calculated diffusion coefficients under two different assumptions: that the total observed abundances equal (i) 100% and (ii) 25% of the Ar initially present.

Results of the latter case and the controlled temperatures of each heating step are shown for one of the aliquots as an Arrhenius plot in Fig. S4b; the assumption of complete Ar extraction results in a nearly identical plot (not shown) except with values shifted upwards by ~ 3 natural log units of D/a^2 . In both aliquots, both ^{39}Ar and ^{37}Ar produce linear Arrhenius correlation at temperatures $< 800^\circ\text{C}$ and a more precise measure of activation energy (E_a) than achievable with the *Husain and Schaeffer* [1975] dataset. By estimating the total Ar content, we repeated this calculation for each aliquot under each assumption and using each isotope. In all eight cases (two Ar isotopes \times two aliquots \times two assumed total Ar abundances), the kinetic parameters are within the following bounds: $E_a = 217.1$ kJ/mol and $\ln(D_0/a^2) = 8.4 \ln(\text{s}^{-1})$ (assuming 100%); and $E_a = 216.7$ kJ/mol and $\ln(D_0/a^2) = 5.58 \ln(\text{s}^{-1})$ (assuming 25%). These two constants are far more precisely determined but nevertheless within error of those inferred by *Garrick-Bethell et al.* [2009] from the data of *Husain and Schaeffer* [1975]. Since our objective is to place an upper bound on the temperature of different scenarios, we focus on the latter values (derived from Fig. S3a, c), which we consider to be the most restrictive (i.e.,

requiring the highest temperatures at all time). We therefore present thermal models using these values (Fig. S3), although we show that this assumption introduces a small uncertainty in the final temperature constraints (Fig. S3d).

Since both the $^{40}\text{Ar}/^{39}\text{Ar}$ and $^{38}\text{Ar}/^{37}\text{Ar}$ spectra show little evidence for thermal disturbance (i.e., little to no discordance), we are able to place conservative upper bounds on various thermal scenarios rather than identify best-fit solutions (e.g., [Shuster *et al.*, 2010]). Previous applications combining both $^{40}\text{Ar}/^{39}\text{Ar}$ and $^{38}\text{Ar}/^{37}\text{Ar}$ thermochronometry of lunar samples have found both radiogenic ^{40}Ar and cosmogenic ^{38}Ar distributions to be internally consistent and well explained by daytime heating near the lunar surface (Shea *et al.*, 2012; Suavet *et al.* 2013). Here, we use a similar strategy as these previous studies and explore the upper bound on duration-temperature conditions required to thermally disturb the $^{40}\text{Ar}/^{39}\text{Ar}$ and $^{38}\text{Ar}/^{37}\text{Ar}$ spectra that are observed to be concordant. Using models for production and diffusion of radiogenic ^{40}Ar [Shuster *et al.*, 2010; Suavet *et al.*, 2013], we show these temperature bounds calculated for a range of reheating durations modeled at 3.9 Ga and 142 Ma (Fig. S3d).

Appendix A3

Cosmogenic neon thermochronology methods

During the step-degassing diffusion experiment, a neutron-irradiated anorthite fragment with a spherically equivalent radius of 296 μm was heated over 97 consecutive heating steps, including three retrograde heating cycles, to temperatures between 100 and 1050 $^{\circ}\text{C}$ and lasting between 0.5 and 10 hours (Table S5). We used the gas purification and mass spectrometric measurement techniques described in [Tremblay *et al.*, 2014a]. Thirteen room temperature procedural blanks measured over the course of the experiment were subtracted from the measurement time zero intercepts; average blank corrections were 0.05×10^6 atoms for ^{21}Ne and 1.5×10^6 atoms for ^{22}Ne . The MAP-215 sector field mass spectrometer in the BGC Noble Gas Thermochronometry Lab used to conduct these measurements cannot resolve $^{22}\text{Ne}^+$ from $^{44}\text{CO}_2^{++}$. However, we found that the $\text{CO}_2^+/\text{CO}_2^{++}$ was constant over the H_2 partial pressure range in the stepwise degassing experiment, and that the average signals on $m/e = 44$ for room-temperature blanks and heating steps are equal. Therefore, we accounted for the $^{44}\text{CO}_2^{++}$ interference in the blank correction described above. No isobaric interference corrections were necessary for ^{21}Ne . Aliquots of a manometrically-calibrated air standard were also analyzed after approximately every fifth heating step to determine neon sensitivities of the mass spectrometer, which we found to be constant over the pressure range of the analyses. During the measurements of naturally-occurring neon in 76535 anorthite (Table S6), we corrected for interferences on ^{22}Ne from $^{44}\text{CO}_2^{++}$ and ^{20}Ne from $^{40}\text{Ar}^{++}$ by introducing a ^{39}Ar spike during neon analyses as described by [Balco and Shuster, 2009].

Supplementary Figure Captions

Figure S1. AF demagnetization of simulated MC and HC components in subsample 1. (A) Stereographic projection of AF demagnetization of 0.2 μT bias field ARMs applied

in the direction of the HC component (ARM1, peak AC field of 290 mT), and putative MC component (ARM2, peak AC field of 100 mT). Remanence directions after applying ARM1 and ARM2 are shown as blue stars, as is the inferred HC direction (anisotropy corrected). The directions of the applied fields for ARM1 and ARM2 are shown as diamonds, with dashed lines representing 25° error circles (the errors are large due to difficulty orienting the sample). The red line shows the great circle connecting ARM1 and ARM2. Open and closed symbols represent projections on upper and lower hemispheres, respectively. **(B)** Same data as (A) but in orthographic projection. Closed and open symbols represent projections onto the north-east and up-east planes, respectively

Figure S2. Equal area stereographic projection of AF demagnetization of a simulated HC component and weak IRM for subsample 2. Open and closed symbols represent projections on upper and lower hemispheres, respectively. The ARM was applied in the direction of the HC component (a bias field of 10 μ T in a peak AC field of 290 mT), and an IRM (13 mT) was subsequently applied in the direction of the LC component. The remanence after application of the ARM and IRM are shown as blue stars, as is the HC direction (anisotropy corrected). The directions of the applied fields for ARM and IRM are shown as diamonds, with dashed lines representing 25° error circles (the errors are large due to difficulty orienting the sample). The black triangle shows the HC direction before anisotropy correction.

Figure S3. $^{40}\text{Ar}/^{39}\text{Ar}$ and $^{38}\text{Ar}/^{37}\text{Ar}$ thermochronology of 76535. **(A)** The observed (points) and the predicted (colored lines) $^{38}\text{Ar}/^{37}\text{Ar}$ spectrum calculated for production and diffusion of cosmogenic ^{38}Ar since the apparent ^{38}Ar exposure age of ~ 142 Ma assuming the most restrictive estimate of Ar diffusion kinetics in **(B)**. The observed $^{38}\text{Ar}/^{37}\text{Ar}$ ratios (and corresponding exposure ages shown on right hand axis) ± 1 standard deviation are plotted against the cumulative release fraction of ^{37}Ar . The inset shows a reduced chi squared misfit statistic calculated between isothermal holding at different temperatures over the complete duration of exposure. Note that most low temperature models produce an identical misfit that is obstructed by the data, which require the effective temperature to have been $< 170^\circ\text{C}$ since 142 Ma. **(B)** Arrhenius plot showing calculated diffusion coefficients (D) normalized to the diffusion domain radius (a) ± 1 standard deviation plotted against the absolute temperature (T) of each stepped heating extraction of aliquot b. Similar results (not shown) were calculated for aliquot a. The line is a linear regression to all extractions below 800°C (filled points) used to model the open system behavior of radiogenic and cosmogenic Ar in **(A)** and **(C)**. **(C)** The observed (points) and the predicted (colored lines) $^{40}\text{Ar}/^{39}\text{Ar}$ spectrum calculated for diffusion of radiogenic ^{40}Ar for different values of Dt/a^2 beginning at 142 Ma. The observed $^{40}\text{Ar}/^{39}\text{Ar}$ ratios (R) ± 1 standard deviation are normalized to the ratio (R_{plateau}) that corresponds to the apparent plateau age of 4249 Ma. The reduced chi squared misfit statistic (inset) calculated for several values of Dt/a^2 requires that 76535 was not heating above a duration-temperature pair corresponding to $\log_{10}(Dt/a^2) = -17.0$ if reheating took place at 142 Ma. Similar models (not shown) identify a maximum of $\log_{10}(Dt/a^2) = -6.2$ if the reheating event took place at 3900 Ma. **(D)** Upper bounds on duration and temperature for reheating events at 3900 Ma (dashed curves) and 140 Ma (solid curves).

Bold curves assume only 25% of the Ar was released during step heating analysis, and fine curves assume 100 % was released. The square shows the upper bound on the effective temperature during the last 142 Ma derived from (A).

Fig. S4. Observations of neon in 76535 anorthite. Panel A is a three isotope plot that shows the neon isotopic composition of the five anorthite grains we analyzed. Four of the five analyses plot on a mixing line between solar wind neon [Grimberg *et al.*, 2006] and cosmogenic neon as determined by [Lugmair *et al.*, 1976]. Our data are offset to the right from an alternative mixing line between solar wind neon and the nominal cosmogenic neon production rate ratios calculated by [Leya *et al.*, 2001]. However, the uncertainties on these latter cosmogenic production rate calculations are large enough (12%; [Leya *et al.*, 2001]) that they overlap with the Lugmair *et al.* [1976] determination within uncertainty. Analysis *v* plots below both mixing lines, which indicates that neon isotope fractionation occurred during solar wind implantation [Grimberg *et al.*, 2006]. The inset in panel A shows reduced χ^2 misfit statistic calculated for different effective diffusion temperatures (EDTs; [Tremblay *et al.*, 2014b]) as follows:

$$\chi^2 = \frac{1}{n-1} \sum_{i=1}^n \left(\frac{R_{o,i} - R_{p,i}}{\sigma_i} \right)^2$$

Where n is the number of measurements, R_p and R_o are the predicted and observed retention values for each measurement, respectively, and σ is the observed retention uncertainty. We calculated this misfit statistic using the ^{21}Ne and ^{22}Ne diffusion parameters derived from the Arrhenius relationships shown in panel B. We estimated the standard deviations from the EDTs 1.2 units greater than the minima in χ^2 , after Shuster and Cassata [2015]. The weighted mean EDT from these two χ^2 distributions is 75.5 ± 4.2 °C. The Arrhenius relationships shown in panel B were calculated from the ^{21}Ne and ^{22}Ne measurements on a neutron-irradiated fragment of 76535 anorthite using the equations of Fechtig and Kalbitzer [1966] and the uncertainty propagation outlined in Tremblay *et al.* [2014a].

Fig. S5. Relationship between EDT and mean temperature (T_{avg}) through the lunar daily insolation cycle at the Apollo 17 site, calculated using the ^{21}Ne diffusion kinetics for 76535 anorthite and surface temperature measurements reported by Keihm and Langseth [1973].

Supporting Information References

Balco, G., and D. L. Shuster (2009), Production rate of cosmogenic ^{21}Ne in quartz estimated from ^{10}Be , ^{26}Al , and ^{21}Ne concentrations in slowly eroding Antarctic bedrock surfaces, *Earth and Planetary Science Letters*, *281*, 48-58.

Grimberg, A., H. Baur, P. Bochsler, F. Bühler, D. S. Burnett, C. C. Hays, V. S. Heber, A. J. G. Jurewicz, and R. Wieler (2006), Solar Wind Neon from Genesis: Implications for the Lunar Noble Gas Record, *Science*, *314*, 1133-1135.

Keihm, S. J., and M. G. Langseth, Jr. (1973), Surface brightness temperatures at the Apollo 17 heat flow site: Thermal conductivity of the upper 15 cm of regolith, in *Lunar and Planetary Science Conference Proceedings*, edited, p. 2503.

Leya, I., S. Neumann, R. Wieler, and R. Michel (2001), The production of cosmogenic nuclides by GCR-particles for 2 pi exposure geometries, *Meteoritics and Planetary Science*, *36*, 1547-1561.

Lugmair, G. W., K. Marti, J. P. Kurtz, and N. B. Scheinin (1976), History and genesis of lunar troctolite 76535 or: How old is old, in *Lunar and Planetary Science Conference Proceedings*, edited by R. B. Merrill, pp. 2009-2033.

Shuster, D. L., G. Balco, W. S. Cassata, V. A. Fernandes, I. Garrick-Bethell, and B. P. Weiss (2010), A record of impacts preserved in the lunar regolith, *Earth and Planetary Science Letters*, *290*(1-2), 155-165, doi:10.1016/j.epsl.2009.12.016.

Shuster, D. L., and W. S. Cassata (2015), Paleotemperatures at the lunar surfaces from open system behavior of cosmogenic ^{38}Ar and radiogenic ^{40}Ar , *Geochimica et Cosmochimica Acta*, *155*, 154-171.

Suavet, C., B. P. Weiss, W. S. Cassata, D. L. Shuster, J. Gattacceca, L. Chan, I. Garrick-Bethell, J. W. Head, T. L. Grove, and M. D. Fuller (2013), Persistence and origin of the lunar core dynamo, *Proceedings of the National Academy of Science*, *110*, 8453-8458.

Tikoo, S. M., B. P. Weiss, J. Buz, E. A. Lima, E. K. Shea, G. Melo, and T. L. Grove (2012), Magnetic fidelity of lunar samples and implications for an ancient core dynamo, *Earth and Planetary Science Letters*, *337*, 93-103.

Tremblay, M. M., D. L. Shuster, and G. Balco (2014a), Cosmogenic noble gas paleothermometry, *Earth and Planetary Science Letters*, *400*, 195-205.

Tremblay, M. M., D. L. Shuster, and G. Balco (2014b), Diffusion kinetics of ^3He and ^{21}Ne in quartz and implications for cosmogenic noble gas paleothermometry, *Geochimica et Cosmochimica Acta*, *142*, 186-204.

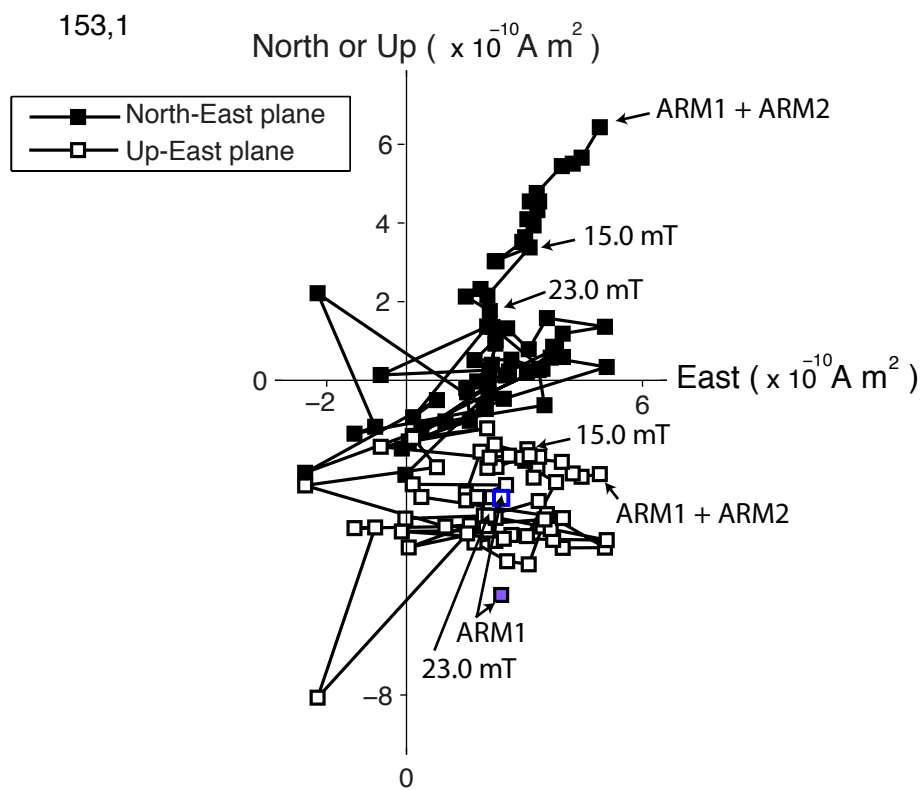
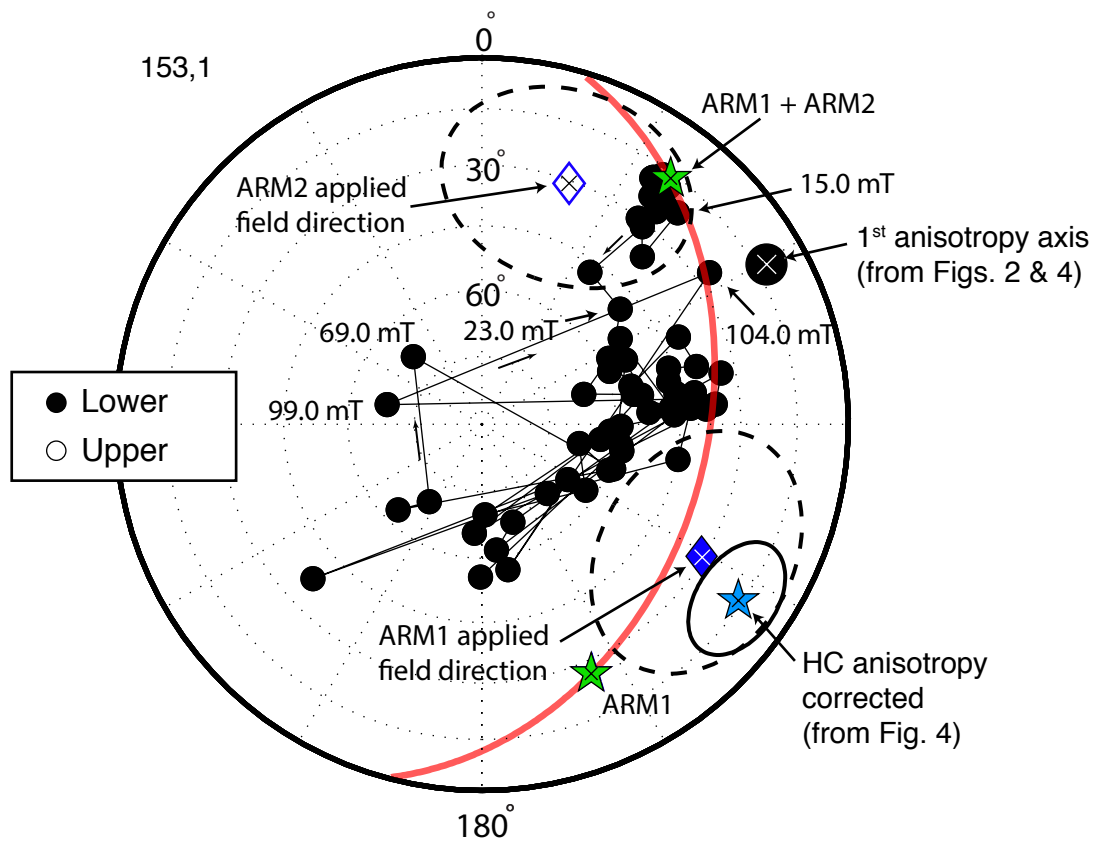


Figure S1

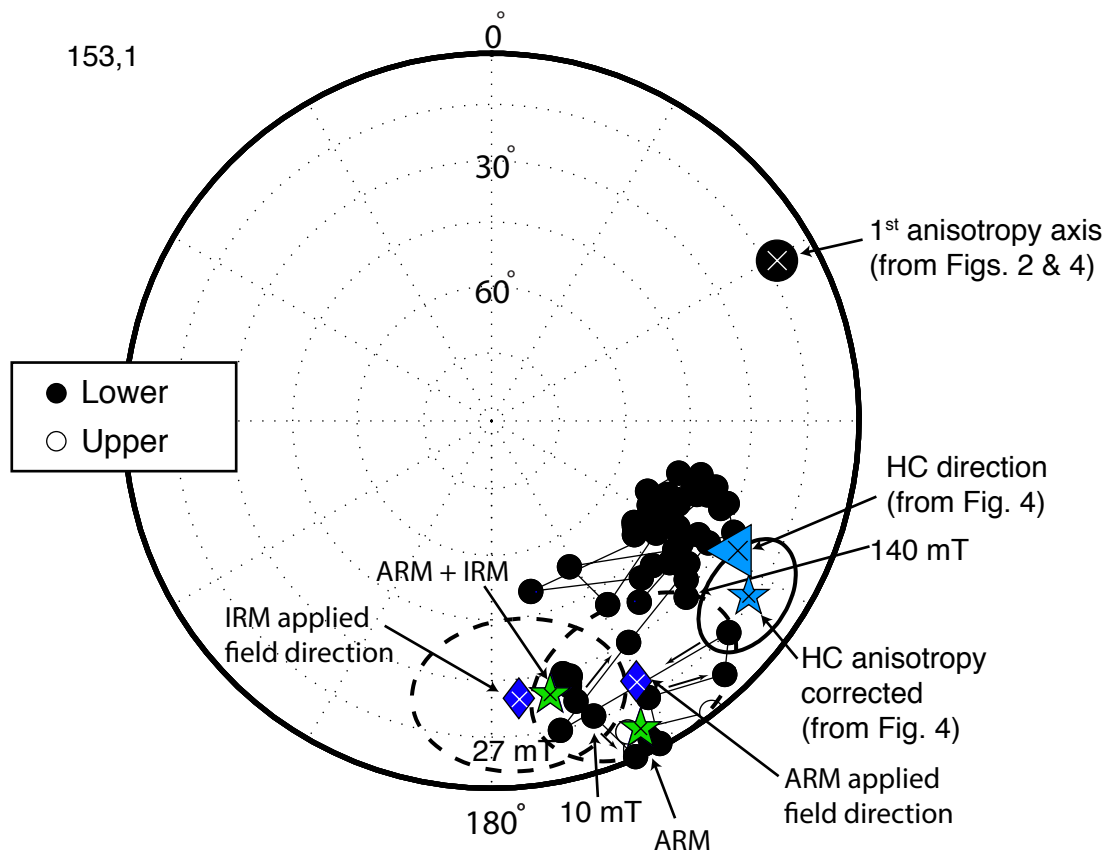


Figure S2

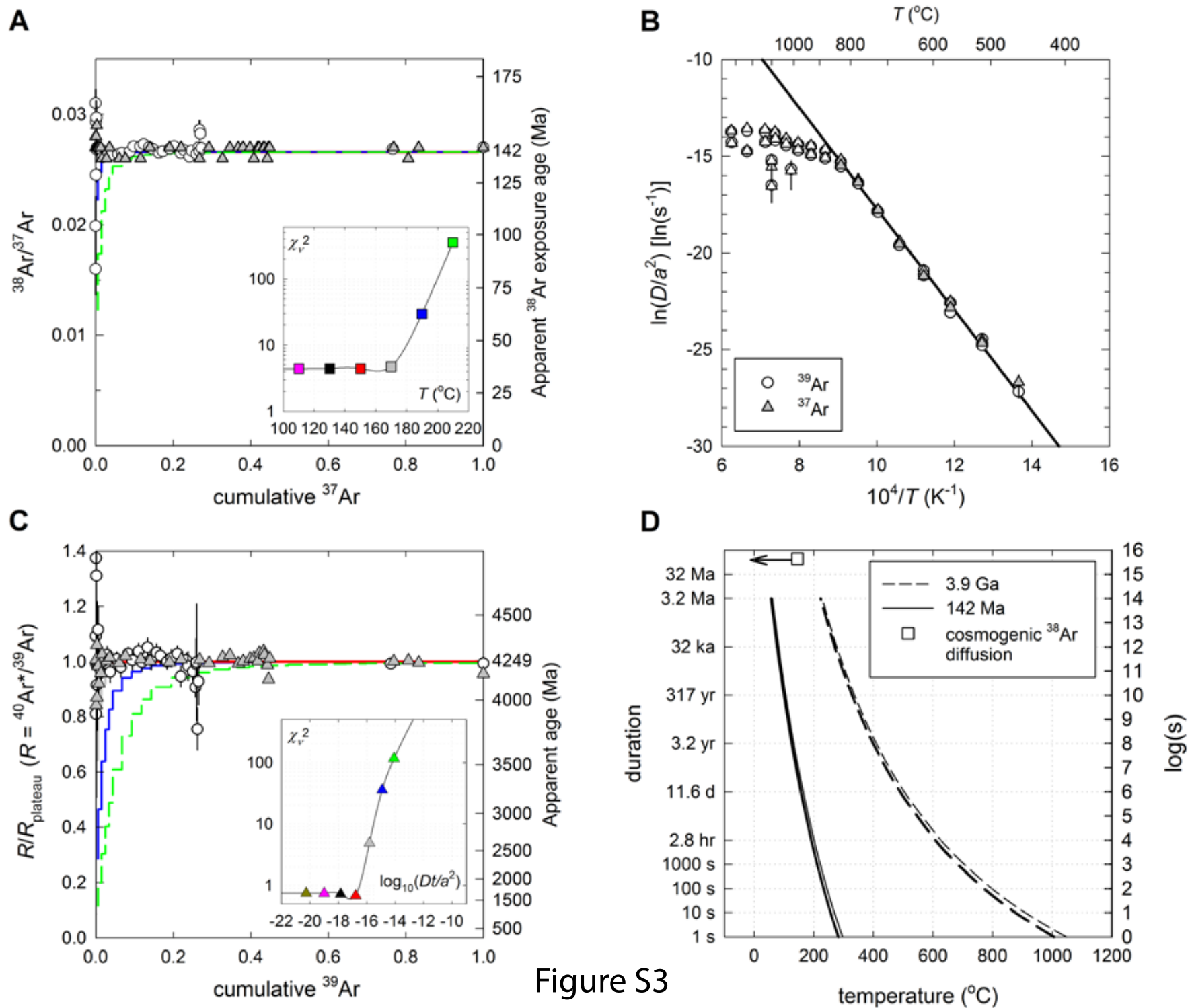
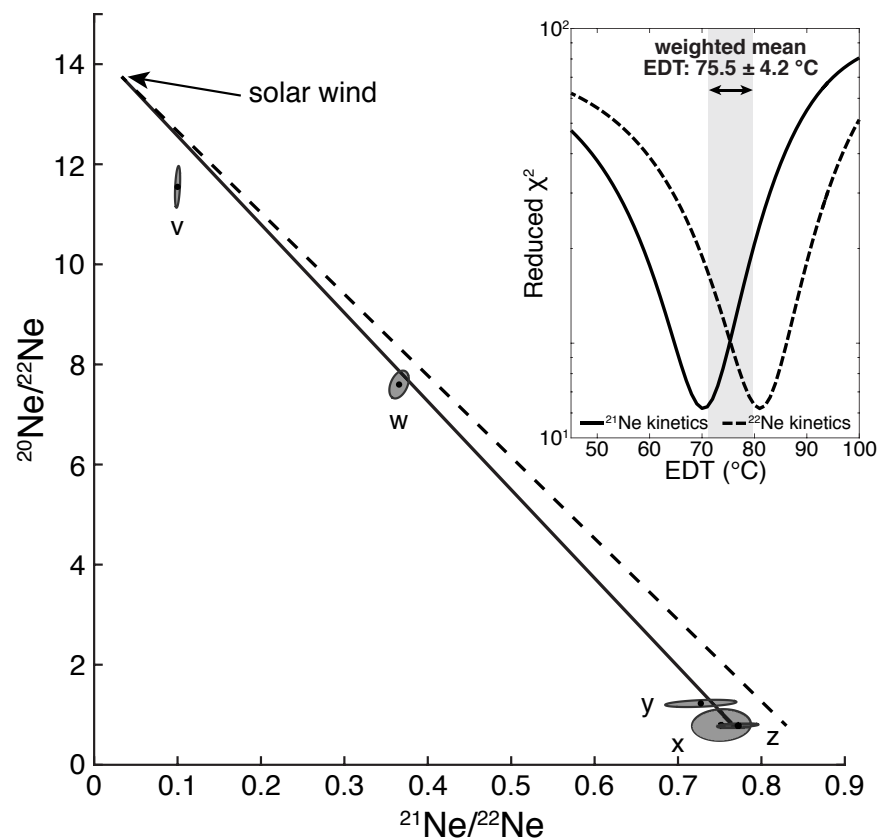


Figure S3

A

— mixing line, cosmogenic component of Lugmair et al. (1976) - - - mixing line, cosmogenic component calculated from Leya et al. (2001)

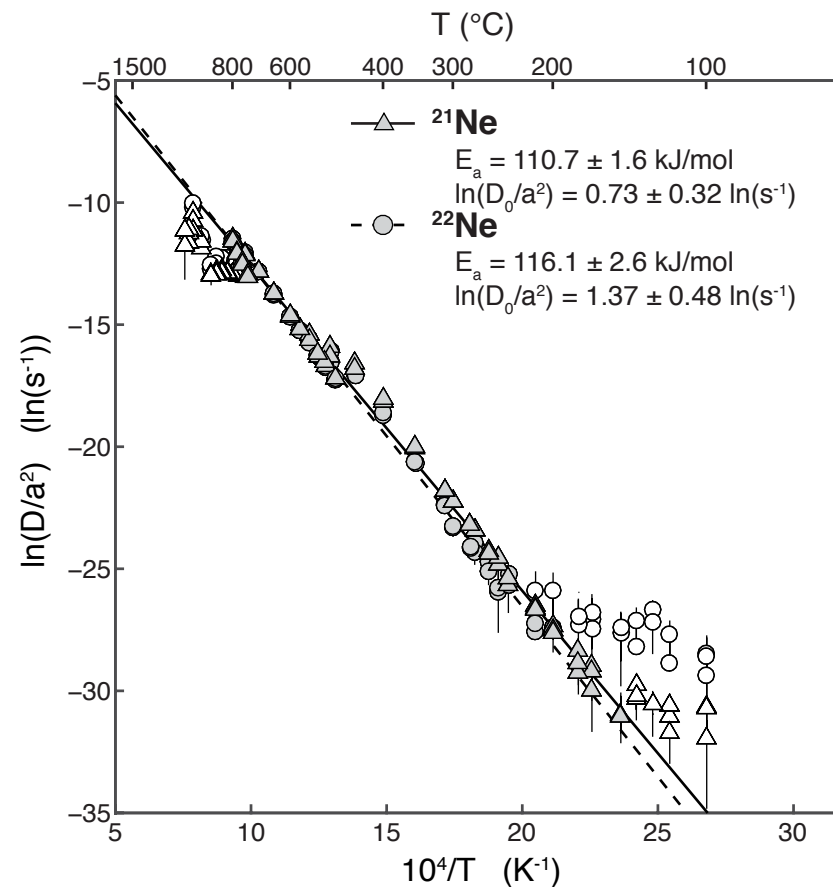
B

Figure S4

○—○ Apollo 17 surface temperature data,
Keihm and Langseth (1973)

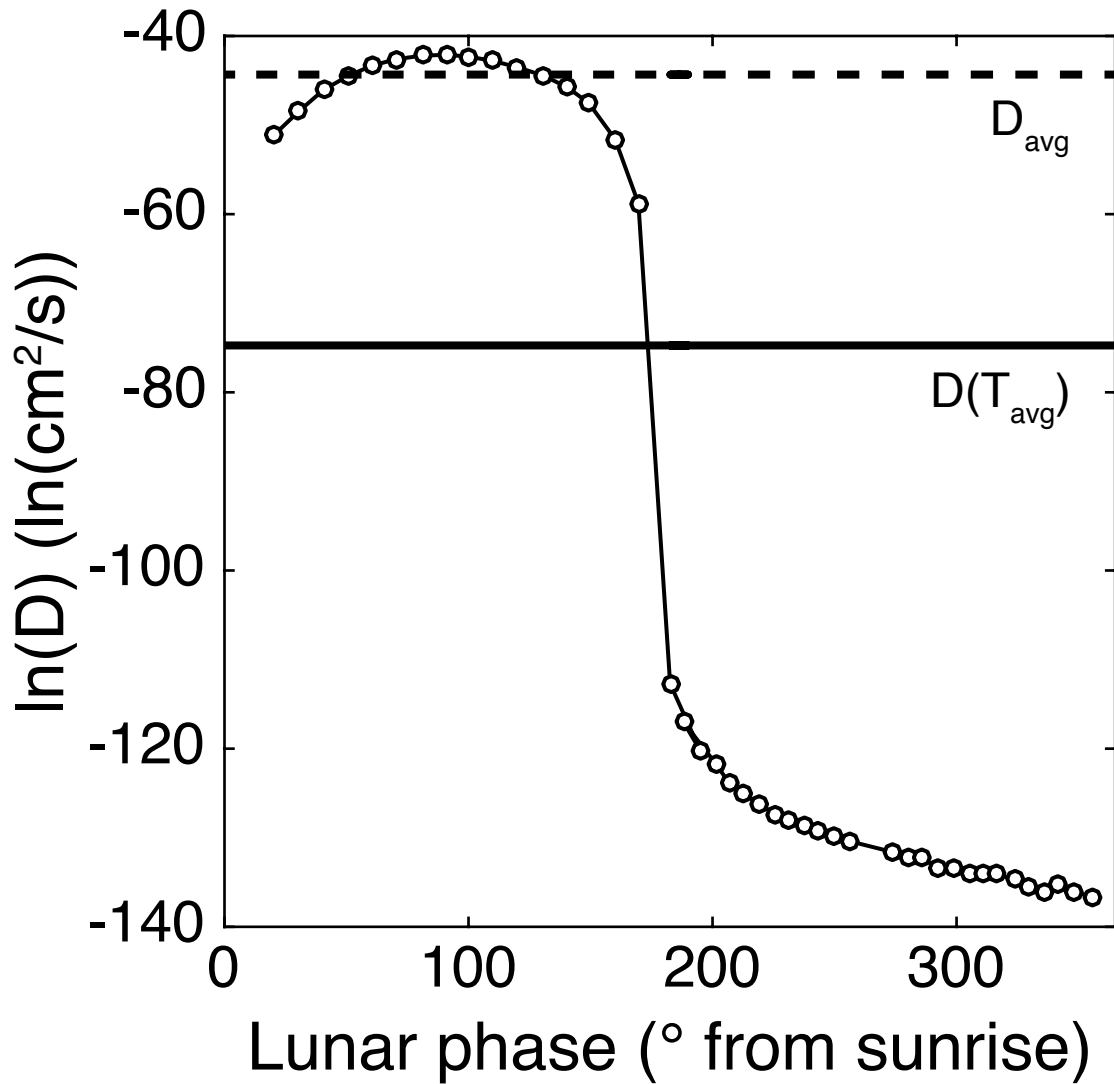
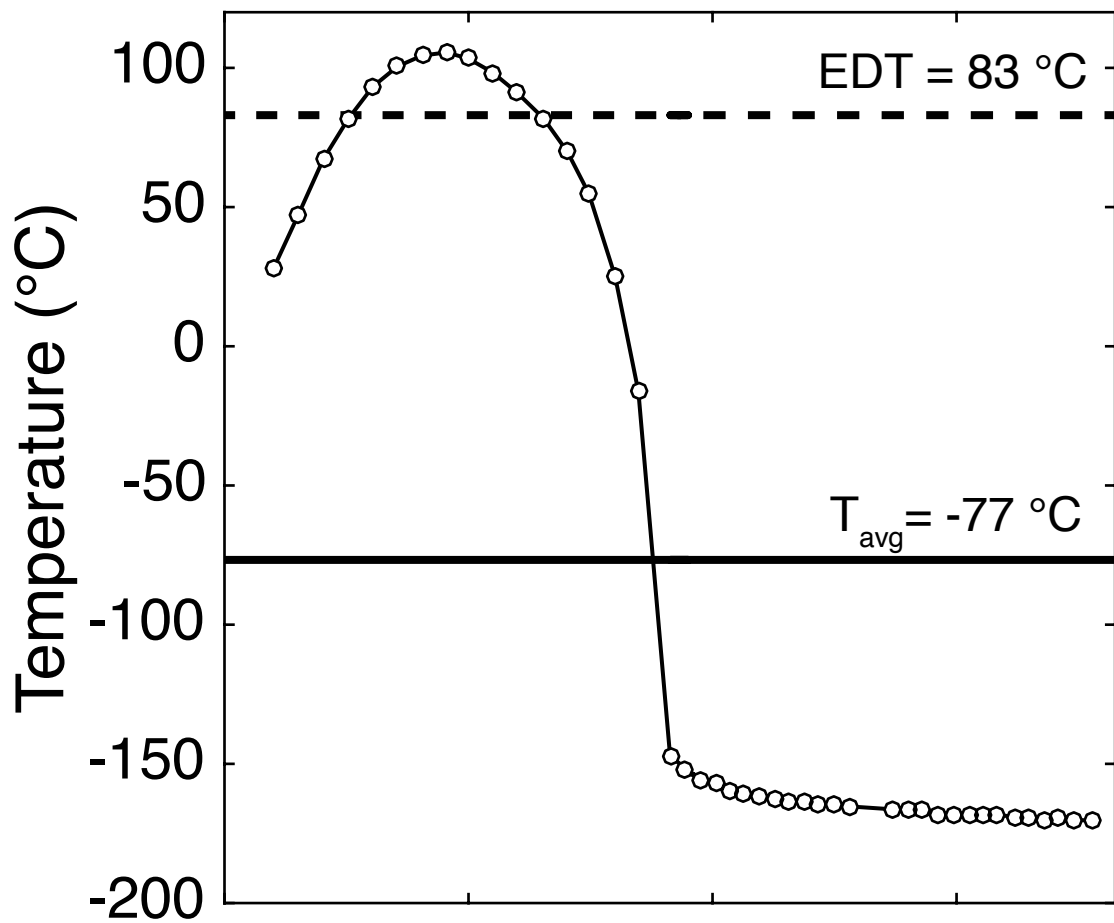


Figure S5

Table S1. AF demagnetization data for sample 76535,153,1

AF step (mT)	Declination (°)	Inclination (°)	Moment (Am ²)
NRM	181.4	47.9	3.90E-09
1.5	182.2	47.9	3.90E-09
2.0	182.5	48.0	3.90E-09
2.5	183.0	48.1	3.90E-09
3.0	182.0	48.0	3.86E-09
3.5	182.8	48.2	3.79E-09
4.0	182.2	47.6	3.62E-09
4.5	182.4	48.4	3.45E-09
5.0	183.5	48.6	3.28E-09
5.5	182.5	48.7	3.04E-09
6.0	181.3	49.1	2.96E-09
6.5	181.3	49.1	2.72E-09
7.0	173.5	49.8	2.55E-09
7.5	171.2	50.5	2.35E-09
8.0	168.5	50.0	2.16E-09
8.5	163.3	49.1	1.97E-09
9.0	168.1	49.9	1.73E-09
9.5	172.7	50.6	1.46E-09
10.0	174.9	50.9	1.27E-09
10.5	165.9	52.9	1.11E-09
11.0	154.7	53.7	1.00E-09
11.5	145.3	57.2	8.79E-10
12.0	133.7	53.8	8.10E-10
12.5	114.0	52.3	7.14E-10
13.0	107.3	47.4	6.93E-10
13.5	106.0	46.7	6.00E-10
14.0	92.3	48.3	5.13E-10
14.5	88.3	46.1	5.01E-10
15.0	79.1	33.1	6.31E-10
15.5	79.3	37.0	5.23E-10
16.0	81.6	37.0	5.22E-10
16.5	86.9	42.3	4.63E-10
17.0	80.1	36.0	6.63E-10
17.5	76.3	29.8	7.28E-10
18.0	79.0	27.2	7.11E-10
18.5	77.9	33.6	7.18E-10
19.0	80.9	35.4	7.05E-10
19.5	82.3	34.4	6.22E-10
20.0	87.0	38.9	6.14E-10
20.5	89.7	36.6	7.22E-10
21.0	84.1	30.9	6.82E-10
21.5	86.1	31.5	7.44E-10
22.0	90.8	35.4	6.92E-10
22.5	87.7	30.1	6.60E-10
23.0	89.8	35.4	6.50E-10
23.5	79.3	43.3	6.35E-10
24.0	77.0	53.2	5.40E-10
24.5	81.5	55.3	6.07E-10
25.0	76.3	53.0	6.23E-10
26.0	82.1	51.3	6.78E-10
27.0	81.9	56.7	6.28E-10
28.0	84.7	59.8	6.03E-10
29.0	71.4	65.3	5.54E-10
30.0	77.1	57.3	6.11E-10
31.0	71.0	55.1	6.14E-10
32.0	72.7	46.2	6.60E-10
33.0	74.1	45.9	6.22E-10
34.0	75.9	48.5	5.66E-10
35.0	72.5	41.5	6.73E-10
36.0	72.2	49.2	5.37E-10
37.0	65.1	45.9	5.46E-10

38.0	67.0	36.8	6.12E-10
39.0	70.6	41.1	6.01E-10
40.0	74.2	41.0	6.67E-10
41.0	65.4	39.9	6.84E-10
42.0	59.9	46.8	5.97E-10
43.0	47.9	65.1	5.03E-10
44.0	324.5	75.3	4.24E-10
45.0	48.6	66.2	4.25E-10
46.0	49.9	53.8	5.27E-10
47.0	55.1	41.7	7.13E-10
48.0	312.3	71.2	4.64E-10
49.0	15.8	74.1	5.19E-10
50.0	51.4	37.9	7.42E-10
51.0	58.2	41.5	7.60E-10
52.0	53.6	40.9	7.70E-10
53.0	55.2	39.7	7.72E-10
54.0	58.9	39.2	8.06E-10
55.0	63.0	48.5	7.33E-10
56.0	64.0	47.5	7.22E-10
57.0	68.3	47.4	7.52E-10
58.0	74.0	49.9	7.52E-10
59.0	72.8	43.2	8.46E-10
60.0	70.2	54.5	7.62E-10
61.0	70.3	63.4	6.89E-10
62.0	71.7	71.0	6.21E-10
63.0	71.9	44.1	8.56E-10
64.0	73.0	63.2	6.84E-10
65.0	77.6	70.5	5.89E-10
66.0	70.1	62.7	6.36E-10
67.0	112.3	84.8	6.15E-10
68.0	74.0	76.1	6.15E-10
69.0	56.1	68.6	6.61E-10
70.0	67.5	47.1	7.72E-10
71.0	82.0	61.5	6.88E-10
72.0	68.9	60.5	7.14E-10
73.0	63.9	47.7	7.14E-10
74.0	70.7	51.6	6.24E-10
75.0	63.8	48.5	7.08E-10
76.0	63.2	55.3	6.52E-10
77.0	61.8	71.9	5.78E-10
78.0	325.9	85.9	5.72E-10
79.0	73.7	75.0	5.79E-10
80.0	256.3	78.3	5.73E-10
81.0	71.2	64.6	6.15E-10
82.0	68.5	57.9	5.87E-10
83.0	89.1	70.9	5.14E-10
84.0	90.3	56.9	6.25E-10
85.0	96.5	77.0	4.96E-10
95.0	100.1	38.9	3.51E-10
105.0	59.2	48.6	3.03E-10
115.0	60.7	44.6	3.71E-10
125.0	230.7	67.2	2.21E-10
135.0	279.0	72.8	2.47E-10
145.0	253.1	48.9	3.66E-10
155.0	184.7	58.0	7.20E-11
175.0	105.2	24.4	3.53E-10
185.0	109.6	26.1	4.44E-10
205.0	134.4	28.7	4.43E-10
215.0	114.4	27.9	4.09E-10
225.0	110.7	15.8	6.07E-10
235.0	129.2	42.2	4.32E-10
245.0	120.5	29.7	4.76E-10
255.0	124.2	19.7	2.95E-10

265.0	109.1	13.1	4.96E-10
275.0	120.2	31.8	7.02E-10
285.0	133.2	16.1	3.91E-10
290.0	115.3	19.9	4.64E-10

Table S2. AF demagnetization data for sample 76535,153,2

AF step (mT)	Declination (°)	Inclination (°)	Moment (Am ²)
NRM	162.4	40.8	4.51E-09
1.5	163.7	42.5	4.42E-09
2.0	164.3	43.1	4.39E-09
2.5	165.3	43.5	4.41E-09
3.0	166	43.3	4.39E-09
3.5	165.8	42.3	4.26E-09
4.0	166.6	42.6	4.10E-09
4.5	165.9	41.0	3.86E-09
5.0	164.3	40.6	3.68E-09
5.5	160.5	40.5	3.33E-09
6.0	159.9	40.0	3.12E-09
6.5	158.8	38.9	2.83E-09
7.0	158	38.7	2.52E-09
7.5	155.7	37.2	2.29E-09
8.0	153.8	36.2	2.02E-09
8.5	153.7	35.1	1.72E-09
9.0	150.8	30.3	1.59E-09
9.5	149.7	28.7	1.34E-09
10.0	147.5	23.7	1.20E-09
10.5	145.6	23.5	1.07E-09
11.0	148	23.6	1.02E-09
11.5	147.1	19.8	1.05E-09
12.0	147.4	18.9	8.73E-10
12.5	139.5	20.3	8.82E-10
13.0	138.3	18.1	8.90E-10
13.5	140.3	21.5	8.75E-10
14.0	135.7	18.6	8.39E-10
14.5	137	15.6	8.82E-10
15.0	139.1	14.1	8.81E-10
15.5	140.2	15.6	8.88E-10
16.0	138.1	18.6	8.96E-10
16.5	138.8	15.3	8.77E-10
17.0	141.2	11.0	9.23E-10
17.5	139.7	15.2	8.32E-10
18.0	135.4	19.0	7.02E-10
18.5	137.4	15.8	7.28E-10
19.0	131.7	20.1	7.08E-10
19.5	132.4	16.8	6.30E-10
20.0	132.4	13.5	8.34E-10
20.5	133.6	17.5	7.89E-10
21.0	134.5	15.3	7.94E-10
21.5	135.4	17.2	7.94E-10
22.0	136.2	12.3	9.00E-10
22.5	137.2	18.3	7.71E-10
23.0	136.3	19.4	7.32E-10
23.5	141.1	12.6	6.97E-10
24.0	144.3	14.7	5.06E-10
24.5	141.5	12.1	5.94E-10
25.0	148.3	12.5	6.59E-10
26.0	139.8	16.5	6.19E-10
27.0	140.5	13.4	5.99E-10
28.0	136.8	10.5	7.15E-10
29.0	140.5	9.9	6.77E-10
30.0	140.1	8.1	7.03E-10
31.0	138.4	7.6	6.88E-10
32.0	140.7	12.6	6.96E-10
33.0	144.8	14.3	6.87E-10
34.0	142.9	7.3	7.04E-10
35.0	138.5	12.4	7.79E-10
36.0	137.4	6.2	7.80E-10
37.0	140	11.1	7.37E-10

38.0	140.2	9.3	6.93E-10
39.0	138.2	8.2	7.59E-10
40.0	136.3	18.4	6.20E-10
41.0	139.5	6.9	7.51E-10
42.0	137	5.0	7.49E-10
43.0	138.5	6.1	7.74E-10
44.0	140	8.3	7.30E-10
45.0	137	0.7	7.39E-10
46.0	139.8	7.1	5.90E-10
47.0	143.5	4.8	5.97E-10
48.0	138.7	10.3	6.57E-10
49.0	140.5	11.7	6.42E-10
50.0	141.9	11.0	8.75E-10
51.0	138.8	7.5	8.13E-10
52.0	132.4	11.5	6.75E-10
53.0	137.3	12.2	7.39E-10
54.0	129.7	13.0	6.40E-10
55.0	127.8	14.2	7.55E-10
56.0	130.9	13.4	7.07E-10
57.0	130.6	13.1	7.81E-10
58.0	132.7	10.3	8.38E-10
59.0	133.5	13.7	6.90E-10
60.0	132.1	13.9	7.18E-10
61.0	135.3	13.6	6.31E-10
62.0	132.2	13.1	6.95E-10
63.0	130.8	12.7	6.70E-10
64.0	130.3	11.9	7.04E-10
65.0	129.9	17.1	6.53E-10
66.0	127.4	15.3	6.75E-10
67.0	128.7	14.0	5.27E-10
68.0	136.5	16.2	4.92E-10
69.0	130.1	13.4	5.44E-10
70.0	128.2	12.2	5.90E-10
71.0	131.4	17.9	5.98E-10
72.0	134.6	11.6	4.70E-10
73.0	132	15.6	6.26E-10
74.0	134.9	8.8	6.85E-10
75.0	160.3	3.6	4.71E-10
76.0	158.3	12.1	4.52E-10
77.0	166.1	0.8	4.23E-10
78.0	152	4.2	6.03E-10
79.0	155.5	4.3	5.69E-10
80.0	161.6	-1.6	5.33E-10
81.0	158.2	1.0	6.01E-10
82.0	150.5	4.1	5.44E-10
83.0	144.3	8.6	6.09E-10
84.0	159.8	0.2	4.81E-10
85.0	175.5	-0.2	4.30E-10
95.0	156.9	7.0	4.01E-10
105.0	155.7	16.5	3.82E-10
115.0	153	15.5	2.95E-10
125.0	143.2	0.1	4.44E-10
135.0	148.3	-9.3	2.71E-10
145.0	137.8	0.0	4.25E-10
155.0	139.4	11.6	4.75E-10
165.0	135	5.5	3.72E-10
175.0	128.1	7.0	3.56E-10
185.0	134.2	19.3	1.93E-10
195.0	129.1	-1.0	2.87E-10
205.0	149.3	-1.8	1.61E-10
215.0	106.3	-30.3	1.29E-10
225.0	117.7	-25.4	8.16E-11
235.0	135.4	-3.6	3.59E-10

245.0	130.4	-1.7	7.35E-11
255.0	141.3	-0.3	2.52E-10
265.0	153.9	-45.4	1.16E-10
275.0	127.3	18.7	1.40E-10
285.0	129.9	-16.0	1.41E-10
290.0	130.3	-39.0	1.66E-10

Table S3. AF demagnetization data for sample 76535,153,3

AF step (mT)	Declination (°)	Inclination (°)	Moment (Am ²)
NRM	168.2	56.3	8.18E-10
1.5	167.4	56.0	8.16E-10
2.0	167.0	56.3	8.13E-10
2.5	167.2	56.2	8.13E-10
3.0	166.4	55.5	8.02E-10
3.5	168.7	56.0	7.76E-10
4.0	167.8	55.5	7.52E-10
4.5	170.7	54.9	7.35E-10
5.0	168.4	53.4	6.79E-10
5.5	168.6	53.7	6.54E-10
6.0	170.6	51.0	6.01E-10
6.5	173.8	48.7	5.44E-10
7.0	173.3	50.2	5.12E-10
7.5	173.0	49.3	4.25E-10
8.0	175.0	45.1	3.84E-10
8.5	177.3	40.9	3.29E-10
9.0	174.6	40.3	3.05E-10
9.5	171.3	37.3	2.43E-10
10.0	163.8	36.7	2.20E-10
10.5	160.1	31.7	2.04E-10
11.0	159.4	30.7	1.94E-10
11.5	156.6	36.6	1.75E-10
12.0	158.2	31.8	1.61E-10
12.5	152.0	30.0	1.51E-10
13.0	150.4	32.2	1.37E-10
13.5	153.0	28.4	1.37E-10
14.0	148.5	23.0	1.18E-10
14.5	154.9	17.5	1.25E-10
15.0	152.2	22.3	1.34E-10
15.5	155.5	28.0	1.31E-10
16.0	156.0	19.5	1.39E-10
16.5	158.8	20.6	1.19E-10
17.0	153.6	20.7	1.20E-10
17.5	161.5	31.2	1.01E-10
18.0	154.4	35.4	1.13E-10
18.5	145.2	20.9	1.17E-10
19.0	142.0	26.7	1.00E-10
19.5	136.0	24.2	1.02E-10
20.0	137.6	17.3	9.80E-11
20.5	140.8	22.2	9.24E-11
21.0	141.0	20.0	1.07E-10
21.5	138.9	15.4	1.04E-10
22.0	139.6	14.5	1.16E-10
22.5	141.6	0.6	1.23E-10
23.0	137.9	-3.0	1.21E-10
23.5	141.3	-9.7	1.33E-10
24.0	135.8	-12.0	1.13E-10
24.5	124.8	8.8	1.42E-10
25.0	119.0	6.6	1.04E-10
26.0	127.2	3.2	1.18E-10
27.0	122.1	0.5	1.26E-10
28.0	118.4	-0.8	1.06E-10
29.0	116.6	-1.2	1.09E-10
30.0	114.0	-3.8	1.03E-10
31.0	119.9	3.6	1.09E-10
32.0	125.1	4.2	8.91E-11
33.0	118.8	3.0	9.40E-11
34.0	116.6	-2.3	1.01E-10
35.0	109.6	-0.6	1.26E-10
36.0	110.9	-7.8	1.23E-10
37.0	120.2	-3.4	1.18E-10

38.0	119.9	-1.4	1.06E-10
39.0	135.5	2.7	9.60E-11
40.0	122.3	0.0	1.08E-10
41.0	129.8	-2.2	1.21E-10
42.0	125.8	-1.7	1.16E-10
43.0	122.0	-2.9	1.20E-10
44.0	120.7	-6.7	1.09E-10
45.0	118.9	1.1	1.17E-10
46.0	115.7	-1.2	1.17E-10
47.0	106.7	-11.3	1.10E-10
48.0	101.8	-4.0	1.20E-10
49.0	110.5	-6.1	1.28E-10
50.0	106.5	-9.5	1.32E-10
51.0	103.9	11.0	1.22E-10
52.0	122.0	1.5	1.31E-10
53.0	123.8	5.3	1.35E-10
54.0	122.4	13.5	1.34E-10
55.0	128.0	-0.9	1.30E-10
56.0	121.2	-0.3	1.42E-10
57.0	123.0	3.5	1.36E-10
58.0	122.7	3.2	1.38E-10
59.0	132.7	3.0	1.40E-10
60.0	121.0	-4.4	1.45E-10
61.0	122.6	10.7	1.50E-10
62.0	119.2	1.6	1.32E-10
63.0	126.4	5.0	1.30E-10
64.0	126.6	8.5	1.36E-10
65.0	125.2	9.2	1.36E-10
66.0	120.9	0.2	1.27E-10
67.0	124.0	2.6	1.25E-10
68.0	120.3	6.6	1.11E-10
69.0	117.3	-4.1	1.18E-10
70.0	118.6	14.7	1.11E-10
71.0	124.3	16.7	9.13E-11
72.0	118.3	40.9	9.49E-11
73.0	121.5	36.7	1.04E-10
74.0	121.3	42.4	9.60E-11
75.0	120.1	35.6	1.03E-10
76.0	122.0	21.9	1.08E-10
77.0	126.4	37.3	9.97E-11
78.0	131.0	34.7	1.09E-10
79.0	115.3	27.5	8.86E-11
80.0	121.1	32.9	1.07E-10
81.0	115.7	32.2	9.92E-11
82.0	119.6	40.7	1.09E-10
83.0	113.2	39.8	1.03E-10
84.0	117.2	40.1	9.22E-11
85.0	106.4	35.3	9.71E-11
95.0	130.7	46.4	1.10E-10
105.0	120.7	52.0	1.29E-10
115.0	134.5	38.1	1.40E-10
125.0	138.4	42.5	1.17E-10
135.0	134.6	46.0	1.17E-10
145.0	138.7	56.8	1.10E-10
155.0	139.6	66.1	1.37E-10
165.0	131.6	54.4	1.01E-10
175.0	118.8	50.5	6.46E-11
185.0	146.8	55.2	8.39E-11
205.0	115.1	38.6	7.01E-11
215.0	118.7	19.7	6.88E-11
225.0	85.1	49.3	5.96E-11
235.0	112.8	8.1	4.78E-11
245.0	116.4	26.2	3.27E-11

255.0	119.5	14.2	7.14E-11
265.0	120.6	-21.2	4.95E-11
275.0	134.4	-22.1	5.99E-11
285.0	107.4	26.7	5.49E-11
290.0	151.2	3.8	4.29E-11

Table S4: Argon Analytical Details

COMPLETE ⁴⁰ Ar/ ³⁹ Ar INCREMENTAL HEATING RESULTS														
#	Temp (°C)	⁴⁰ Ar ± 1σ	³⁹ Ar ± 1σ	³⁸ Ar ± 1σ	³⁷ Ar ± 1σ	³⁶ Ar ± 1σ	⁴⁰ Ar* (%)	³⁹ Ar _k (%)	³⁶ Ar _{cos} (%)	³⁸ Ar _{trap} (%)	³⁶ Ar _{Cl} (%)	³⁶ Ar _{cos} (%)	³⁶ Ar _{trap} (%)	Ca/K Apparent Age ± 1s (Ma)
76535-a whole-rock fragment														
1	460 °C	0.06981 ± 0.00064	0.00014 ± 0.00004	0.00080 ± 0.00002	0.02781 ± 0.00058	0.00060 ± 0.00002	100.0	85.9	97.7	0.0	0.0	100.0	0.0	463.1 5095 ± 636
2	459 °C	0.03665 ± 0.00049	0.00007 ± 0.00003	0.00041 ± 0.00001	0.01443 ± 0.00056	0.00033 ± 0.00002	100.0	86.3	96.7	3.1	0.0	78.4	20.4	448.3 5060 ± 938
3	513 °C	0.13961 ± 0.00084	0.00043 ± 0.00004	0.00176 ± 0.00002	0.06079 ± 0.00077	0.00125 ± 0.00002	100.0	90.1	98.4	1.3	0.0	89.4	9.3	308.3 4266 ± 184
4	513 °C	0.06428 ± 0.00061	0.00023 ± 0.00004	0.00082 ± 0.00001	0.02932 ± 0.00062	0.00060 ± 0.00001	100.0	91.3	97.8	1.8	0.0	85.5	13.2	270.1 3977 ± 302
5	566 °C	0.26036 ± 0.00080	0.00092 ± 0.00004	0.00344 ± 0.00003	0.12393 ± 0.00104	0.00250 ± 0.00003	100.0	90.6	98.1	1.5	0.0	87.5	11.2	291.0 4026 ± 83
6	566 °C	0.13446 ± 0.00084	0.00040 ± 0.00004	0.00180 ± 0.00002	0.06168 ± 0.00083	0.00130 ± 0.00002	100.0	89.2	98.2	1.5	0.0	87.8	10.9	341.9 4351 ± 203
7	619 °C	0.50359 ± 0.00102	0.00160 ± 0.00005	0.00685 ± 0.00004	0.24727 ± 0.00141	0.00510 ± 0.00004	100.0	89.3	97.8	1.9	0.0	85.1	13.6	339.5 4228 ± 60
8	619 °C	0.28467 ± 0.00100	0.00096 ± 0.00005	0.00381 ± 0.00002	0.13868 ± 0.00088	0.00285 ± 0.00003	100.0	89.9	97.7	2.0	0.0	84.5	14.2	315.6 4122 ± 90
9	673 °C	1.03318 ± 0.00153	0.00336 ± 0.00006	0.01411 ± 0.00006	0.51263 ± 0.00325	0.01060 ± 0.00006	100.0	89.4	97.6	2.1	0.0	84.1	14.6	334.2 4185 ± 34
10	673 °C	0.64337 ± 0.00104	0.00197 ± 0.00005	0.00861 ± 0.00004	0.31808 ± 0.00168	0.00640 ± 0.00005	100.0	88.8	97.8	1.9	0.0	85.3	13.4	356.7 4297 ± 49
11	724 °C	2.20100 ± 0.00202	0.00690 ± 0.00008	0.03017 ± 0.00007	1.11394 ± 0.00718	0.02287 ± 0.00007	100.0	88.8	97.5	2.2	0.0	83.3	15.4	356.6 4259 ± 25
12	724 °C	1.51473 ± 0.00172	0.00468 ± 0.00007	0.02058 ± 0.00007	0.75222 ± 0.00492	0.01470 ± 0.00005	100.0	88.8	98.4	1.3	0.0	89.3	9.4	354.4 4279 ± 30
13	775 °C	4.48222 ± 0.00361	0.01415 ± 0.00013	0.06116 ± 0.00011	2.28644 ± 0.01176	0.04290 ± 0.00011	100.0	88.8	98.7	1.0	0.0	91.1	7.5	356.8 4247 ± 22
14	775 °C	2.89296 ± 0.00281	0.00893 ± 0.00009	0.03870 ± 0.00009	1.47656 ± 0.01064	0.02696 ± 0.00007	100.0	88.5	98.8	0.9	0.0	91.8	6.7	366.1 4288 ± 24
15	829 °C	7.25954 ± 0.00431	0.02261 ± 0.00016	0.09673 ± 0.00018	3.67104 ± 0.01446	0.06658 ± 0.00015	100.0	88.7	99.1	0.7	0.0	93.1	5.4	358.7 4269 ± 19
16	827 °C	4.51606 ± 0.00391	0.01414 ± 0.00011	0.06049 ± 0.00015	2.26263 ± 0.01637	0.04106 ± 0.00010	100.0	88.9	99.2	0.5	0.0	94.6	3.9	352.8 4257 ± 20
17	879 °C	9.59085 ± 0.00501	0.03003 ± 0.00019	0.12710 ± 0.00020	4.65417 ± 0.04192	0.08500 ± 0.00017	100.0	89.2	99.4	0.3	0.0	96.2	2.3	340.4 4251 ± 17
18	879 °C	5.64594 ± 0.00371	0.01754 ± 0.00014	0.07447 ± 0.00015	2.76918 ± 0.01222	0.05055 ± 0.00010	100.0	89.0	99.2	0.5	0.0	94.6	3.9	347.5 4268 ± 19
19	931 °C	9.06408 ± 0.00461	0.02823 ± 0.00021	0.11935 ± 0.00020	4.49722 ± 0.02527	0.08014 ± 0.00014	100.0	88.9	99.3	0.3	0.0	95.8	2.7	351.2 4286 ± 19
20	930 °C	4.54478 ± 0.00371	0.01429 ± 0.00013	0.05978 ± 0.00014	2.23455 ± 0.01380	0.03979 ± 0.00015	100.0	89.1	99.4	0.2	0.0	96.8	1.7	343.8 4265 ± 21
21	982 °C	6.57407 ± 0.00541	0.02031 ± 0.00015	0.08679 ± 0.00018	3.26895 ± 0.02303	0.05798 ± 0.00012	100.0	88.8	99.4	0.3	0.0	96.4	2.1	355.2 4281 ± 19
22	982 °C	3.54966 ± 0.00351	0.01088 ± 0.00012	0.04679 ± 0.00011	1.73756 ± 0.00769	0.03150 ± 0.00009	100.0	88.9	99.3	0.4	0.0	95.5	3.0	352.0 4292 ± 25
23	1033 °C	4.16704 ± 0.00331	0.01313 ± 0.00014	0.05531 ± 0.00013	2.05610 ± 0.01194	0.03747 ± 0.00010	100.0	89.1	99.2	0.5	0.0	94.8	3.7	344.3 4243 ± 24
24	1032 °C	2.36474 ± 0.00291	0.00741 ± 0.00010	0.03174 ± 0.00009	1.17802 ± 0.00694	0.02124 ± 0.00008	100.0	88.9	99.4	0.3	0.0	96.2	2.3	350.5 4256 ± 28
25	1082 °C	3.29397 ± 0.00311	0.01024 ± 0.00006	0.04435 ± 0.00011	1.65791 ± 0.01447	0.02996 ± 0.00010	100.0	88.7	99.2	0.4	0.0	95.2	3.4	357.6 4272 ± 22
26	1083 °C	1.74473 ± 0.00152	0.00541 ± 0.00010	0.02335 ± 0.00009	0.87612 ± 0.00549	0.01571 ± 0.00007	100.0	88.7	99.3	0.4	0.0	95.6	2.9	357.5 4276 ± 38
27	1132 °C	1.93165 ± 0.00172	0.00604 ± 0.00008	0.02573 ± 0.00008	0.95156 ± 0.00628	0.01729 ± 0.00007	100.0	89.0	99.3	0.4	0.0	95.7	2.8	346.8 4257 ± 27
28	1132 °C	0.87512 ± 0.00114	0.00267 ± 0.00006	0.01363 ± 0.00005	0.43484 ± 0.00312	0.00782 ± 0.00004	100.0	88.7	99.3	0.4	0.0	95.7	2.8	360.4 4306 ± 45
29	1231 °C	1.95757 ± 0.00202	0.00594 ± 0.00007	0.02660 ± 0.00009	0.97961 ± 0.00551	0.01822 ± 0.00007	100.0	88.5	99.0	0.6	0.0	93.6	4.9	365.2 4316 ± 25
30	1231 °C	0.43923 ± 0.00122	0.00134 ± 0.00006	0.00552 ± 0.00004	0.20328 ± 0.00141	0.00377 ± 0.00004	100.0	89.4	99.1	1.5	0.0	94.1	4.5	333.4 4295 ± 78
31	1329 °C	1.38028 ± 0.00171	0.00438 ± 0.00008	0.01857 ± 0.00008	0.70182 ± 0.00434	0.01275 ± 0.00005	100.0	88.9	99.0	0.7	0.0	93.4	5.2	353.1 4235 ± 34
32	1330 °C	0.60826 ± 0.00114	0.00202 ± 0.00005	0.00792 ± 0.00005	0.29370 ± 0.00162	0.00536 ± 0.00004	100.0	89.9	99.2	0.5	0.0	94.9	3.7	317.7 4147 ± 50
33	>1300 °C	0.56434 ± 0.00083	0.00175 ± 0.00005	0.00747 ± 0.00004	0.27767 ± 0.00204	0.00498 ± 0.00003	100.0	89.0	99.4	0.3	0.0	96.5	2.0	350.0 4274 ± 74
34	>1300 °C	59.75866 ± 0.01900	0.18723 ± 0.00055	0.80470 ± 0.00071	29.88402 ± 0.12937	0.53620 ± 0.00060	100.0	88.9	99.4	0.2	0.0	96.7	1.9	351.9 4256 ± 14
35	>1300 °C	7.11567 ± 0.00432	0.02224 ± 0.00016	0.09465 ± 0.00017	3.57034 ± 0.01299	0.06270 ± 0.00014	100.0	88.8	98.5	0.1	0.0	97.3	1.2	354.2 4262 ± 18
36	>1300 °C	5.16426 ± 0.00461	0.01621 ± 0.00012	0.06867 ± 0.00015	2.52098 ± 0.01561	0.04602 ± 0.00010	100.0	89.2	99.4	0.3	0.0	96.0	2.5	341.8 4248 ± 28
37	1394 °C	31.11041 ± 0.06500	0.10145 ± 0.00039	0.41880 ± 0.00058	15.45525 ± 0.14067	0.27961 ± 0.00045	100.0	89.4	99.4	0.3	0.0	96.4	2.1	333.9 4182 ± 15
76535-b whole-rock fragment														
1	459 °C	0.01219 ± 0.00046	0.00002 ± 0.00004	0.00011 ± 0.00001	0.00555 ± 0.00040	0.00016 ± 0.00001	100.0	84.4	82.3	17.3	0.0	62.7	62.7	521.8 5071 ± 3122
2	459 °C	0.00919 ± 0.00041	0.00003 ± 0.00004	0.00012 ± 0.00001	0.00529 ± 0.00047	0.00015 ± 0.00001	100.0	86.5	86.6	13.1	0.0	44.2	54.9	438.4 4389 ± 2478
3	513 °C	0.04688 ± 0.00062	0.00011 ± 0.00004	0.00061 ± 0.00001	0.01906 ± 0.00057	0.00046 ± 0.00001	100.0	87.8	97.5	2.3	0.0	83.0	15.9	390.0 4771 ± 635
4	513 °C	0.02209 ± 0.00047	0.00008 ± 0.00004	0.00029 ± 0.00001	0.00956 ± 0.00044	0.00026 ± 0.00001	100.0	92.0	95.0	4.6	0.0	71.0	28.1	245.2 3905 ± 869
5	567 °C	0.08897 ± 0.00068	0.00028 ± 0.00005	0.00117 ± 0.00002	0.04585 ± 0.00076	0.00097 ± 0.00002	100.0	88.8	95.9	3.7	0.0	74.9	23.8	357.4 4233 ± 293
6	567 °C	0.04908 ± 0.00065	0.00011 ± 0.00004	0.00067 ± 0.00002	0.02171 ± 0.00049	0.00053 ± 0.00002	100.0	86.5	96.8	3.0	0.0	79.0	19.9	441.0 4692 ± 715
7	619 °C	0.17371 ± 0.00094	0.00060 ± 0.00004	0.00256 ± 0.00002	0.09155 ± 0.00078	0.00216 ± 0.00002	100.0	89.3	95.7	4.0	0.0	73.6	25.3	337.2 4101 ± 120
8	619 °C	0.09813 ± 0.00069	0.00031 ± 0.00004	0.00134 ± 0.00002	0.04772 ± 0.00064	0.00113 ± 0.00002	100.0	89.4	95.8	3.9	0.0	74.0	24.9	334.3 4218 ± 249
9	671 °C	0.36066 ± 0.00094	0.00104 ± 0.00005	0.00536 ± 0.00003	0.18729 ± 0.00124	0.00488 ± 0.00003	100.0	87.5	94.3	5.5	0.0	67.0	32.0	404.6 4424 ± 86
10	672 °C	0.21646 ± 0.00098	0.00070 ± 0.00003	0.00317 ± 0.00003	0.11186 ± 0.00105	0.00277 ± 0.00003	100.0	88.8	95.0	4.7	0.0	70.3	28.6	354.1 4213 ± 108
11	725 °C	0.79252 ± 0.00133	0.00261 ± 0.00007	0.01193 ± 0.00006	0.42081 ± 0.00417	0.01063 ± 0.00005	100.0	88.8	94.6	5.0	0.0	68.8	30.1	356.4 4179 ± 50
12	724 °C	0.53748 ± 0.00123	0.00171 ± 0.00005	0.00777 ± 0.00003	0.28886 ± 0.00150	0.00607 ± 0.00004	100.0	88.2	97.0	2.7	0.0	80.5	18.2	375.7 4246 ± 52
13	777 °C	1.66156 ± 0.00161	0.00517 ± 0.00008	0.02428 ± 0.00008	0.90213 ± 0.00532	0.01810 ± 0.00007	100.0	87.9	97.8	1.9	0.0	84.9	13.8	388.9 4286 ± 31
14	777 °C	1.05636 ± 0.00113	0.00347 ± 0.00007	0.01493 ± 0.00006	0.55991 ± 0.00336	0.01053 ± 0.00005	100.0	88.8	98.6	1.1	0.0	90.6	8.0	356.3 4182 ± 40
15	829 °C	2.40999 ± 0.00232	0.00759 ± 0.00010	0.03417 ± 0.00009	1.28041 ± 0.00686	0.02331 ± 0.00008	100.0	88.3	99.1	0.6	0.0	94.1	4.5	374.6 4260 ± 28
16	829 °C	1.41509 ± 0.00133	0.00457 ± 0.00009	0.01978 ± 0.00006	0.73893 ± 0.00648	0.01344 ± 0.00005	100.0	88.8	99.2	0.5	0.0	94.5	4.0	357.3 4210 ± 37
17	880 °C	2.67318 ± 0.00251	0.00824 ± 0.00009	0.03665 ± 0.00009	1.36489 ± 0.00839	0.02520 ± 0.00009	100.0	88.5	99.0	0.7	0.0	93.2	5.3	367.0 4291 ± 24
18	880 °C	1.49871 ± 0.00133	0.00470 ± 0.00009	0.02024 ± 0.00007	0.73999 ± 0.00497	0.01382 ± 0.00006	100.0	89.1	99.1	0.6	0.0	94.0	4.6	346.5 4252 ± 37
19	931 °C	2.25298 ± 0.00252	0.00687 ± 0.00010	0.03066 ± 0.00011	1.12258 ± 0.00690	0.02082 ± 0.00005	100.0	88.6	99.2	0.5	0.0	94.6	4.0	361.1 4304 ± 30

Table S5. Amount of ^{21}Ne and ^{22}Ne released during each heating step for the step degassing diffusion experiment on a neutron-irradiated anorthite from 76535, with analytical uncertainties. All measurements are blank corrected. bdl indicates blank-corrected values that were below detection limit.

Step	Temperature (°C)	Time (hour)	^{21}Ne (10^6 atom)	\pm (10^6 atom)	^{22}Ne (10^6 atom)	\pm (10^6 atom)
1	100.0	2.0	0.17	0.06	0.41	0.38
2	100.0	4.0	0.12	0.04	0.58	0.37
3	100.0	6.0	0.04	0.04	0.45	0.37
4	120.0	2.0	0.03	0.04	bdl	bdl
5	120.0	4.0	0.08	0.04	0.18	0.37
6	120.0	6.0	0.03	0.04	0.68	0.36
7	140.0	2.0	0.07	0.04	bdl	bdl
8	140.0	4.0	0.07	0.04	0.22	0.37
9	140.0	6.0	0.11	0.04	0.83	0.39
10	170.0	2.0	0.10	0.05	0.24	0.39
11	170.0	4.0	0.07	0.05	0.57	0.37
12	170.0	6.0	0.20	0.06	0.39	0.36
13	150.0	6.0	0.03	0.04	0.30	0.36
14	150.0	8.0	0.04	0.05	0.47	0.38
15	130.0	8.0	0.06	0.04	0.84	0.35
16	130.0	10.0	bdl	bdl	0.57	0.37
17	180.0	2.0	0.12	0.04	bdl	bdl
18	180.0	4.0	0.09	0.05	0.20	0.35
19	180.0	6.0	0.18	0.05	0.40	0.35
20	200.0	2.0	0.24	0.05	0.36	0.36
21	200.0	4.0	0.35	0.07	0.15	0.36
22	200.0	6.0	0.38	0.06	0.23	0.35
23	214.9	2.0	0.34	0.07	0.32	0.38
24	215.0	4.0	0.54	0.08	0.12	0.40
25	215.0	6.0	0.65	0.07	0.24	0.38
26	249.9	1.0	0.59	0.09	0.15	0.37
27	250.0	2.0	1.26	0.08	0.34	0.37
28	275.0	1.0	1.57	0.11	0.97	0.38
29	274.9	2.0	2.45	0.13	1.17	0.38
30	300.0	1.0	3.04	0.13	1.50	0.41
31	299.9	2.0	4.54	0.25	2.68	0.44
32	280.0	4.0	2.72	0.16	1.89	0.43
33	280.0	6.0	3.56	0.20	2.64	0.45
34	260.0	6.0	1.11	0.09	1.26	0.37
35	260.0	7.0	1.14	0.10	0.94	0.38
36	240.0	7.0	0.30	0.06	0.84	0.37
37	240.0	8.0	0.45	0.08	0.58	0.39
38	310.0	1.0	1.89	0.15	1.87	0.41
39	309.9	2.0	3.58	0.19	3.17	0.49
40	349.8	1.0	8.32	0.36	7.82	0.53
41	350.0	2.0	13.70	0.50	12.23	0.70

42	399.9	0.5	16.61	0.55	15.66	0.76
43	399.8	1.0	26.57	0.79	26.11	0.80
44	449.9	0.5	41.65	1.19	44.52	1.12
45	449.8	1.0	47.30	1.29	56.17	1.51
46	499.9	0.5	45.65	1.27	56.14	1.42
47	500.0	1.0	48.32	1.36	57.74	1.50
48	549.9	0.5	47.29	1.40	57.85	1.44
49	549.9	1.0	64.16	1.77	78.00	1.88
50	525.0	1.5	41.71	1.30	52.70	1.23
51	525.0	2.0	50.22	1.54	60.75	1.71
52	510.0	2.5	37.54	1.14	47.80	1.15
53	510.0	3.0	41.75	1.25	53.93	1.51
54	489.9	3.5	27.56	0.79	34.16	1.05
55	490.0	4.0	29.62	0.90	36.63	1.03
56	514.9	2.5	32.69	1.00	42.17	1.15
57	530.0	2.0	34.59	1.05	43.56	1.26
58	574.9	0.5	23.01	0.74	28.42	0.99
59	574.9	1.0	42.59	1.23	53.83	1.44
60	599.9	0.5	32.47	1.00	41.91	1.15
61	600.0	1.0	63.58	1.79	79.35	1.94
62	648.5	0.5	72.83	2.13	88.58	2.04
63	649.5	1.0	125.00	3.42	157.98	3.31
64	699.2	0.5	126.78	3.46	158.75	3.59
65	699.6	1.0	207.38	5.53	257.41	5.22
66	749.2	0.5	169.09	4.64	214.35	4.37
67	749.3	1.0	240.55	6.47	302.36	5.95
68	799.3	0.5	173.02	4.71	215.97	4.33
69	799.7	1.0	226.88	6.11	287.37	5.59
70	779.8	1.5	157.26	4.24	198.83	3.98
71	779.7	2.0	134.08	3.65	167.80	3.79
72	759.7	2.0	67.30	1.96	84.28	1.92
73	759.9	2.5	55.88	1.60	71.41	1.74
74	739.9	3.0	33.81	0.99	44.01	1.42
75	739.8	3.5	27.23	0.88	34.48	1.07
76	749.8	3.5	20.39	0.65	25.35	0.82
77	774.9	3.5	16.55	0.56	20.73	0.81
78	799.8	2.0	7.82	0.33	10.93	0.51
79	824.3	0.5	1.96	0.12	2.24	0.41
80	824.7	1.0	3.48	0.20	4.24	0.42
81	849.4	0.5	1.79	0.10	1.93	0.40
82	849.7	1.0	3.00	0.16	3.37	0.41
83	874.4	0.5	1.49	0.11	1.55	0.39
84	874.3	1.0	2.40	0.14	2.10	0.38
85	899.4	0.5	1.17	0.12	0.78	0.40
86	899.7	1.0	2.04	0.14	1.66	0.40
87	948.6	0.5	2.89	0.16	1.92	0.41
88	949.7	1.0	5.95	0.26	3.50	0.40
89	999.2	0.5	6.33	0.30	3.26	0.46
90	999.6	1.0	4.87	0.25	2.66	0.41

91	999.6	2.0	2.75	0.13	0.73	0.38
92	1024.8	0.5	0.32	0.06	bdl	bdl
93	1024.9	1.0	0.51	0.07	bdl	bdl
94	1024.9	2.0	0.33	0.07	bdl	bdl
95	1049.8	0.5	0.05	0.04	bdl	bdl
96	1049.9	1.0	0.13	0.04	bdl	bdl
97	1049.9	2.0	0.20	0.05	bdl	bdl

Table S6. Observations of neon in 76535 anorthite. Measured abundances of neon isotopes in aliquots w, x, y, and z are consistent with two-component mixing between cosmogenic and solar wind neon. For these aliquots we calculated the cosmogenic neon abundances. To calculate the total amount of cosmogenic neon produced during 142 ± 3 Ma of exposure, we used the elemental, depth-dependent production rates of cosmogenic neon in Leya et al. (2001) and the composition of 76535 from Dymek et al. (1975). Because we do not know the shielding depth of the specific anorthite grains we analyzed, depth-averaged production rates for each neon isotope were calculated over the maximum dimension of the whole rock sample inferred from photographs (6.5 cm). Cosmogenic neon retention was then calculated by dividing the observed cosmogenic neon abundances by the total amount of cosmogenic neon produced.

Aliquot	²⁰ Ne	±	²¹ Ne	±	²² Ne	±
<i>Measured abundances (10⁶ atoms)</i>						
v (0.74 mg)	306027	6155	2650	42	26500	385
w (1.89 mg)	127928	2586	6155	99	16836	250
x (0.46 mg)	661	187	625	15	831	20
y (2.71 mg)	17266	536	10239	316	14077	363
z (1.68 mg)	5119	158	4995	78	6469	100
<i>Cosmogenic abundances (10⁶ atoms)</i>						
w	5801	442	5862	179	7973	297
x	618	262	625	22	828	25
y	10115	705	10222	409	13572	370
z	4943	312	4995	149	6454	113
<i>Total cosmogenic neon produced during 142 ± 3 Ma of exposure (10⁶ atoms)</i>						
w	7726	970	8292	1041	9954	716
x	1880	236	2018	253	2423	174
y	11078	1390	11890	1492	14273	1026
z	6868	862	7371	925	8848	636
<i>Cosmogenic neon retention</i>						
w	0.75	0.11	0.71	0.09	0.80	0.06
x	0.33	0.15	0.31	0.04	0.34	0.03
y	0.91	0.13	0.86	0.11	0.95	0.07
z	0.72	0.10	0.68	0.09	0.73	0.05